A Substructure Method For Large Scale Magneto-Thermal-Hydrodynamic Flows

(部分分割有限要素法による大規模電磁熱流体解析)

Marie Oshima

(大島まり)

A Substructure Method For Large Scale Magneto-Thermal-Hydrodynamic Flows

（部分分割有限要素法による大規模電磁熱流体解析）

December, 1991

(平成３年１２月)

Marie Oshima

(大島まり)

Table of Contents

Chapter 1

Introduction

1.1 Motivation

The rapid advancement in the last decade of electronic technology is attributed mainly to improvements in semiconductor manufacturing processes. Associated with this recent progress in the microelectronics, the demand for higher economic performances in semiconductors has been increasing, particularly in commercial applications [1.1]. In order to respond to this demand, processes which employ single crystal technologies hope to produce a large diameter monolith which retains favorable single crystal properties [1.1]-[1.3].

In general, Czochralski (CZ) method is widely used for producing a large size single crystal of silicon [1.2]. The phenomena in the Czochralski system during growth of a single crystal is quite complex since hydrodynamics in the melt, heat transfer in the whole Czochralski system and dopant transport from the melt to the crystal interact with one another [1.4]. As the diameter of a single crystal becomes larger, these highly coupled phenomena become more complicated and become more difficult to control. Because of the high temperature of Czochralski system, it is almost impossible to directly measure system parameters. As a result, the numerical simulations is a viable means to study these complex phenomena and to understand relationship between qualities of a single crystal and the processes of a single crystal growth.

There are two approaches to solve the Czochralski melt growth: 1) the global model, which focuses on heat transfer in the system to obtain the macroscopic behavior such as shape of the melt/crystal interface [1.4]-[1.6], and 2) the detailed analyses, which focus on each phenomenon such as thermal hydraulics in the melt or stress-strain behavior of the crystal [1.7]-[1.9]. An axial symmetric analysis using the global model has become a common numerical analysis method. However, the assumptions for the global model are

no longer valid for a large diameter single crystal. Therefore, it is necessary to analyze the detailed behavior of each physical process separately and to integrate them as a whole.

Although the recent improvement in computers and computational techniques allow simulation of highly coupled systems, a three dimensional analysis of an entire Czochralski system is presently not feasible. Among various interactions between qualities of a crystal and the process of single crystal growth, it is recognized that qualities of a single crystal are influenced by the phenomena occurring in the melt during the growth phase. Particularly, the main factors which degrade single crystal qualities are: 1) thermal striations due to the macroscopic oscillation of the flow or temperature near the crystal/melt interface, and 2) inhomogeneous distribution of a large amount of impurities and dopants [1.2],[1.3],[1.9]. This degradation is usually caused in the melt by a certain condition resulting from interaction between natural and forced convection, and thus it is important to control convective flows in the Czochralski crucible. One way to control convective flows in the melt is to impose an electricmagnetic field. Since the silicon melt is an electroconducting fluid, the convection in the melt can be suppressed due to the Lorentz force by imposing a magnetic field [1.10]-[1.12]. Although various types of experiments have been performed, many effects of a magnetic field on the melt are not well understood and remain to be solved. Therefore, primary objective of the thesis is to develop an analysis program for a magneto-thermal-hydraulic flow to simulate the flow patterns and temperature distributions of the melt during growth of a single crystal. Such numerical simulations with and without the presence of the magnetic field will allow the effects of a magnetic field on the melt behavior to be investigated.

Other objectives of the thesis are to develop an effective numerical analysis algorithm specifically for the melt growth process. Because the flow patterns and temperature distributions in the melt are found to be as transient three-dimensional phenomena experimentally, a three-dimensional transient computer program is required for a magneto-thermal-hydrodynamic flow. In case of a magneto-thermal-hydrodynamic flow, the number of degrees of freedom yields to the number of meshes multiplied by a total of six variables, velocities (u_x, u_y, u_z), pressure (P), temperature (T) and electric potential (ϕ). Thus, the analysis tends to become a large scale problem due to high number of degrees of freedom, and computational performance parameters such as memory size and

CPU time increase accordingly with increases in the number of degrees of freedom. To conduct numerical analyses for such a large scale problem, analyses have to be done using a reasonable amount of CPU time and within the allowable memory capacity of the computer.

This thesis developed the numerical analysis algorithm based on the substructure method combined with the MAC time integration scheme by considering an axial symmetric configuration of the Czochralski crucible. The substructure method is applied to solve the Poisson equations for both the pressure and the electric potential in order to minimize memory usage and CPU time required to solve the Poisson equations. In the substructure method, an analysis domain is divided into a number of substructures [1.13]-[1.14]. The global matrix consists of internal variables in the substructure and the boundary invariables on the shared boundaries. If substructures consist of the same geometrical configuration and boundary conditions, the condensed-out matrices for substructures are the same. As a result, both memory and CPU time can be reduced.

Thus, in summary, this thesis focuses on the numerical simulation of the melt during growth of a single crystal and on development of the numerical analysis method specialized to simulate the melt behavior such as the flow patterns and temperature distributions.

1.2 Objectives

The thesis aims to develop an efficient numerical analysis algorithm for a large scale magneto-thermal-hydraulic problem and to simulate silicon melt during growth of a large diameter single crystal in the presence of a magnetic field. The ultimate goal is to obtain a better understanding of the relationship between the quality of a single crystal and the melt during growth of a single crystal through simulations.

The objectives of the thesis are summarized as follows.

(1) The substructure method is proposed as an effective numerical algorithm for a large

scale problem with a large number of degrees of freedom considering the characteristics of the Czochralski crucible geometry.

(2) Computational performance parameters of the substructure method such as memory requirements and CPU time, are investigated by comparing the results with those of the conjugate gradient and the skyline methods.

(3) The simulation of a small diameter single crystal was performed under various operating conditions, and the effects of a magnetic field and rotation speed were investigated.

(4) The simulation of a large diameter crystal was performed and effects on flow patterns and temperature distributions are evaluated.

1.3 Outline of the Thesis

The first chapter describes the motivation and objectives of the thesis, and also explains the outline of the thesis.

Chapter 2 will briefly review the research in melt growth processes and computational fluid dynamics. The first section explains the mechanism of the Czochralski system and the phenomena occurring in the melt during growth of a single crystal. Secondly, the present research situation in the melt growth is summarized, mentioning both of the global model and the detailed melt flow analyses. The most current topics of computational fluid dynamics for large scale problems are also summarized.

Chapter 3 discusses theory and numerical analysis model for a transient magneto-thermal-hydraulic flow in three-dimensions. The governing equations for the fluid and the thermal fields are presented, and derivation of the governing equation for the magnetic field is explained in detail. Following the derivations of the governing equations and the boundary conditions, Chapter 3 presents the discretization of governing equations by finite element methods in space. For the time integration scheme, the MAC (Marker And

Cell) method is used [1.15] so that the discretization of the governing equations in time is described based on the MAC method. Lastly, the finite element matrix equations and the overall flow chart for a magneto-thermal-hydraulic simulation are summarized.

Chapter 4 presents the implementation of the substructure method. When the MAC method is used for time integration in order to incorporate the incompressible condition by splitting velocity and pressure fields, the Poisson equation in terms of the pressure is derived. Similarly, the expression for the electric potential has the form of the Poisson equation. First of all, methods of solving the Poisson equation are summarized based on the characteristics of its global matrix. Considering computational performance in a magneto-thermal-hydraulic flow analysis, the requirements for both memory size and CPU time become the most important factors in solving finite element matrices. In order to improve the computational performance in solving the Poisson equations, the substructure method is introduced by taking advantage of the axisymmetric configuration of Czochralski crucible. Since the analysis domain can be divided into substructures with the same geometry, only one condensed-out matrices of the internal variables in a substructure is required to be stored, which results in reduction in memory size and CPU time. Theory of the substructure method is described with referring to the differences from the domain decomposition method, which is another method to solve a problem by dividing the analysis region into the number of sub-domains [1.16]. Finally, the algorithm based on the substructure method is presented in chapter 4.

Chapter 5 summarizes the analysis results of cavity flows. First, analysis of a cavity flow is presented in order to demonstrate the applicability of the substructure method. The present method assures good correlation with the other analyses which use finite difference method. The memory requirements and CPU time were evaluated by varying the number of substructures. It was found that when the analysis region was divided into more than 3 by 3 in both x- and y- directions, the memory sizes were reduced.

Chapter 6 presents the analysis results of melt flows for both small and large diameter single crystals . First of all, the analysis model and the assumption for the boundary conditions are described. And then, the analyses were performed to simulate melt flows for a small diameter single crystal with one-inch diameter by the conjugate gradient

method. Several boundary conditions were applied by varying rotation speed of crucible and crystal, and also a magnitude and direction of a magnetic field so as to examine their effects on the flow patterns and temperature distributions of the melt. It was found that the effects due to the rotation of the crucible did not give any significant influences on either the flow patterns or the temperature distributions because of dominant effects due to the natural convection. On the contrary, the velocity and temperature were drastically suppressed by imposing a magnetic field and non-axisymmetric flow patterns were observed when the magnetic field was imposed in the horizontal direction.

Before the melt flow analysis for a large-diameter crystal was conducted, memory usage and CPU time were assessed with respect to the number of degrees of freedom based on the results from the cavity flows. As a result, the substructure method with eight-substructure division can reduce the memory size to 1/1000 of the memory size required for the skyline method and also can reduce the CPU time to 1/5 of the CPU time required for the conjugate gradient method. In addition, the correlation for the CPU time are estimated for the conjugate gradient method and the substructure method. The increase in CPU time for the conjugate gradient method can be assumed to behave between 1.5-th and 1.8-th power function of the increase in the number of degrees of freedom. On the other hand, The increase in CPU time for the substructure method can be assumed to be linear to between 1.5 times and 1.9 times increase in the number of degrees of freedom. Finally, analysis for a large diameter single crystal was performed and analysis results are presented.

Chapter 7 presents the summary of the analysis results. This chapter also discusses the recommendations based on the knowledge obtained by the analysis to provide feedback for the future improvement.

Lastly, Chapter 8 states conclusions of the thesis.

[References]

[1. 1] Ogino, M., and Ohashi, H., " Semiconductor Materials"(in Japanese), The Journal of the Institute of Electrical Engineering of Japan, Vol.100, pp.300-305(1988).

[1. 2] Nakaya, W., " Melt Growth for a Large Diameter Single Crystal by Czochralski Method"(in Japanese), Science of Machine, Vol.39, pp.131-134(1987) .

[1. 3] Imaishi, N., and Hozawa, M.," Fluid Mechanics and Heat Transfer in Single Crystal Production"(in Japanese), Chemistry and Chemical Industry, Vol.52, pp.803-807(1988).

[1. 4] Brown, R. A., Kinney, T. A., Sackinger, P. A., and Bornside, D. E., " Toward an Integrated Analysis of Czochralski Growth", Journal of Crystal Growth, Vol.97, pp.99-115(1989).

[1. 5] Sackinger, P. A., Brown, R. A., and Derby, J. J.," A Finite Element Method for Analysis of Fluid Flow, Heat Transfer and Free Interfaces in Czochralski Crystal Growth", International Journal for Numerical Methods in Fluids, Vol.9, pp.453-492(1989).

[1. 6] Tsukada, T., Imishi, N. and Hozawa, M., " Theoretical Study of the Flow and Temperature Fields in CZ Single Crystal Growth", Journal of Chemical Engineering of Japan, Vol.21, pp.184-191(1988).

[1. 7] Langlois, W., and Lee, H. J.," Czochralski Crystal Growth in an Axial Magnetic Field: Effects of Joule Heating", Journal of Crystal Growth, Vol.62, pp.481-486(1983).

[1. 8] Mihelcic, M., and Wingerath, K.," Numerical Simulations of the Czochralski Bulk Flow in an Axial Magnetic Field: Effects on the Flow and Temperature

Oscillations in the Melt", Journal of Crystal Growth, Vol.71, pp.163-168(1985).

[1. 9] Ikuo, S., Tanaka, M., and Nakamura, M., " Numerical Analysis of Thermal Convection in Si Melt During Growth of a Single Crystal"(in Japanese), Yawata Technical Report, Vol.330, pp.37-43(1988).

[1. 10] Hoshikawa, K., and Hirata, H., " Growth of Single Crystals in the Presence of a Magnetic Field" (in Japanese), Journal of Japanese Association of Melt Growth, Vol.27, pp.177-188(1985).

[1. 11] Munakata, T., and Tanasawa, I., " A Study of the Onset of Oscillatory Flow in a Czochralski Growth Melt and Its Suppression by a Magnetic Field", Transactions of the Japan Society of Mechanical Engineers, B-Vol.55, pp.2610-2617(1989).

[1. 12] Mihelcic, M., and Wingerath, K.," Three-Dimensional Simulation of the Czochralski Bulk Flow in a Stationary Transverse Field and in a Vertical Magnetic Field: Effects on the Asymmetry of the Flow and Temperature Distribution in the Si Melt", Journal of Crystal Growth, Vol.82, pp.318-326(1987).

[1.13] Tong, P., and Rossettos, J., Finite Element Method Basic Technique and Implementation, (translated in Japanese by Yagawa G.), Kyouritsu Publisher, Tokyo, Japan(1983).

[1.14] Murata, K., Nataori, R., and Karaki, S., Large Scale Numerical Simulation, Iwanami Publisher, Tokyo, Japan(1990).

[1. 15] Gresho, P. M., et al.," A Modified Finite Element Method For Solving the Time-Dependent Incompressible Navier-Stokes Equations, Part I; Theory ", International Journal of Numerical Methods in Fluids, Vol.4, pp.557-598(1984).

[1. 16] Glowinski, R., et al., " Domain Decomposition Methods For Nonlinear Problems in Fluid Dynamics", Computational Mechanics In applied Mechanics and Engineering", Vol.40, pp.27-109(1983).

[1. 17] Okuda, H., Ph.D Thesis, The University of Tokyo, Department of Nuclear Engineering (in Japanese) (1989).

Chapter 2

Background of Single Crystal Melt Growth and Computational Fluid Dynamics in the Melt Growth

2.1 Introduction

The Czochralski growth technique has been widely applied to produce a single crystal of semiconductor materials such as silicon or refractory oxide crystals used in electronic devices. As a variant of the Czochralski method, the liquid-encapsulated Czochralski (LEC) technique is used for the growth of gallium arsenide (GaAs). Fig. 2.1.1.a) shows the schematic illustration of the Czochralski system [2.1]. For the LEC system, a layer of inert encapsulant , typically boric oxide (B_2O_3), covers the surface of the melt in order to prevent As in the GaAs melt from volatilizing.

In both Czochralski and liquid-encapsulated Czochralski method, the growth process is initiated by dipping a small seed to the surface of a heated pool of the melt contained in a cylindrical crucible as illustrated in Fig. 2.1.1.a). After the crystal radius becomes a desired diameter size by controlling the thermal environment as the seed is raised, the cylindrical single crystal is continued to be pulled vertically as the parameters of the thermal environment are kept constant.

In contrast with simple configuration of the Czochralski system, the physical phenomena in the system are quite complicated. Numerical analysis is becoming an essential means to understand the physical behavior in the Czochralski melt growth. There have been mainly two numerical approaches to solve the Czochralski melt growth. One approach is the global model analysis [2.2]-[2.4] and the other one is the detailed analysis [2.5]-[2.7]. Although the thesis focuses on the detailed analysis, the concept and the outline of the global model analysis are briefly described in Chapter 2 in order to deepen the understanding of the Czochralski melt growth.

Secondly, the background of the detailed analysis in the Czochralski melt growth is summarized. The melt in the Czochralski crucible shows the highly coupled convective flows as schematically illustrated in Fig.2.1.1.b). There are mainly three types of convective flows in the melt: 1) natural convection, which is caused by the temperature differences between the bottom and the top of the crucible, 2) forced convection, which is caused by rotating crystal and crucible, and 3) Marangoni convection, which is caused by the surface tension on the free surface [2.8]. Since the silicon melt is an electroconducting fluid, the convective flows can be controlled by applying a magnetic field. If a magnetic field is imposed to suppress the convection, the effects of the magnetic field has to be considered as a magnetohydrodynamic flow. In general, Marangoni convection is not as dominant as natural and forced convection for a large diameter single crystal [2.9]. Therefore, the thesis focuses on natural and convective flows in the presence of a magnetic field. Chapter 2 explains the effects of an external magnetic field on the melt qualitatively and the current research situation in this field will be described.

Finally, the research on the computational fluid dynamics is briefly summarized. The melt flow requires to develop the transient numerical analysis program in three-dimensions since the convective flows in the melt is recognized to show non-axial symmetric behavior and the temperature oscillation caused by the convective flows is also observed to be transient phenomenon [2.10]. The development of numerical analysis program for a three-dimensional transient problem is quite demanding in aspects of memory and CPU time requirements. In this sense, Chapter 2 summarizes and discusses the most current issues in the computational fluid dynamics, particularly emphasizing on computational analyses of large scale problems.

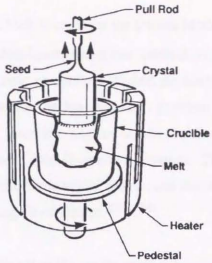

a) The Czcochralski crystal growth configuration[2.1]

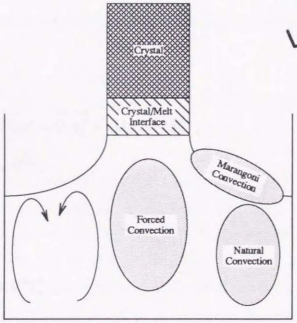

b) Convective flows in the melt during the Czcochralski crystal growth

Fig. 2.1.1 Schematic illustration of convective flows in the melt during the Czochralski crystal growth

2.2 Single Crystal Melt Flow

2.2.1 Analysis of the Czochralski Melt Growth by the Global Model

The global model has been the dominant numerical method in the Czochralski melt growth, aiming to obtain macroscopic characteristics and the long time scale dynamics. In other words, the global model solves the free-boundary problem to define the shape of the crystal and the melt/crystal interface and to obtain field variables such as the temperature distribution in all phases of the Czochralski system. Therefore, it requires to consider the heat transfer in the entire Czochralski system and the interaction between the melt, the crystal and the surrounding environment [2.1]-[2.4].

However, since it is not feasible to solve the entire system precisely, the global model generally simplifies the analysis by assuming a quasi-steady state in the cylindrical coordinate system. The governing equation system used for the global model consists of equations in the melt and the crystal phases and are given respectively as follows [2.11].

In the melt:

$$\vec{\nabla} \cdot \vec{v_l^*} = 0 \ , \tag{2.2.1}$$

$$\vec{v_l^*} \cdot \vec{\nabla}\vec{v_l^*} = -\vec{\nabla}P_l^* - \vec{\nabla} \cdot \vec{\tau_l^*} + Gr\left(T_l^* - 1\right)\vec{e_z} \ , \tag{2.2.2}$$

$$Pr\, \vec{v_l^*} \cdot \vec{\nabla} T_l^* = \nabla^2 T_l^* \ . \tag{2.2.3}$$

In the crystal:

$$Pe\, \vec{e_z} \cdot \vec{\nabla} T_s^* = \nabla^2 T_s^* \ , \tag{2.2.4}$$

where v_l^*, P_l^*, τ_l^*, and T_l^* are the normalized melt velocity, pressure, traction force, and melt temperature , T_s^* is the normalized crystal temperature and e_z is the unit vector in the z-direction. The non-dimensional numbers Gr, Pr, and Pe are the Grashof number, the Prandtl number, and the Peclet number, respectively defined as

$$Gr \equiv \frac{g\,\beta_m\,R_c^3 \Delta T_m}{\nu_m^2}\ , \tag{2.2.5}$$

$$Pr = \frac{\nu_m}{\alpha_m}\ , \tag{2.2.6}$$

$$Pe = \frac{U_g\,R_c}{\alpha_s}\ , \tag{2.2.7}$$

where g is the gravitational acceleration, β_m is the coefficient of thermal expansion, R_c is the crucible radius, ΔT_m is the temperature difference between the crucible wall and the melting point, ν_m is the kinematic viscosity, α_m is the thermal diffusivity in the melt, U_g is the pull rate, and α_s is the thermal diffusivity in the crystal.

The shape of crystal/melt interface, gas/melt interface, and the size of crystal are determined by varying the size of elements on the interface in order to satisfy the requirements that the radiation heat loss from crystal surface becomes equivalent to the sum of latent heat generation and heat coming into the crystal through the crystal/melt interface as well as the interface temperatures may be kept at the melting point isotherm .

The first modelling to solve the governing equations (2.2.1) – (2.2.4) is to neglect convective heat transfer in the melt by assuming conduction-dominated thermal-capillary model (CDTCM) [2.2],[2.11],[2.12].

The methodology developed in the CDTCM has been extended to include more elaborate models by taking account into interactions of radiative heat exchange between the various components of the system or convective flows in the melt. In aspect of radiative heat exchange, diffuse-gray radiation between crystal, melt and crucible was employed by Atherton, et al. [2.13]. Dupret , et al. considered the heat transfer in the entire furnace including the heater and insulations [2.14]. In aspect of the convective melt flow, calculations of the axisymmetric convective flows were introduced to CDTCM as the hydrodynamic thermal-capillary model (HTCM) by Sackinger [2.1],[2.3].

The global model is quite valid to obtain the long time scale dynamics such as changes in the field variables associated with decrease in the melt level, whose time scale is in the

order of hours. As the diameter becomes larger, the interactions between components become more complex. In particular, effects of the convective flows on the crystal becomes significant. The time scale of the convective flows is in the order of a few seconds and the flow pattern shows the three-dimensional profiles. Although the global model is applied to an analysis of large size single crystals [2.15], there is limitation in the global model as long as the quasi-steady state axisymmetric assumption is used. Therefore, it is quite important to develop numerical analysis methods to analyze the detailed behavior in each component to obtain an understanding of the mechanism in the Czochralski melt growth.

2.2.2 Analysis of the Czochralski Melt Flows

On the contrary to the global model, the detailed analysis focuses on specific physical phenomena such as thermal hydraulic behavior in the melt or stress-strain behavior in the crystal. Since the main interest of the thesis is to compute the temperature distribution and the flow pattern in the melt, this section summarizes exclusively the current research situation in the numerical analysis of melt flows, so called "bulk flows" in the Czochralski and the Magnetic Czochralski methods.

First of all, the steady state axisymmetric bulk flows was analyzed by Kobayashi for low values of the Grashof number [2.16]. The time-dependent axisymmetric flow was computed by Langlois [2.17] and the results showed the effects of buoyancy-driven convection and rotation of the crystal and the crucible. Milelcic, et al., extended to the transient three-dimensional analysis by finite difference methods and presented the non-axisymmetric temperature distributions and flow patterns by giving an axisymmetric temperature boundary conditions on the crucible walls [2.18]. The transient bulk flows in three-dimensions were also computed by Sawada [2.7] with including the turbulent model (k-ε model) and the direct simulation method. It was found that the direct simulation method was more valid than the k-ε model to simulate the flow and the temperature fields in the bulk flows.

The research on the Czochralski bulk flow have elucidated various features and effects of the convective flows on the temperature and flow fields in the melt. Yet, the results are difficult to be applied to experimental systems since the analysis are performed under the

given temperature boundary conditions, the size and shape of crystal, which depend on the interactions between convection in the melt and heat transfer through the crystal/melt interface. Therefore, determining the boundary conditions would be the most difficult aspect of the detailed analysis. The desirable approach would be to incorporate the detailed analysis with the global model or the experimental data so as to determine the boundary conditions by the global model or the experimental data and then to perform the detailed analysis.

2.2.3 Analysis of the Czochralski Melt Flows in the Presence of a Magnetic Field

One of the key factors to obtain a high quality single crystal is to control the behavior of temperature and flow fields in the melt. Imposing a magnetic field on the melt, so called the magnetic Czochralski method (MCZ) has been attracted as a potential method to control the melt behavior [2.19]. In particular, since the experiment by Hoshi [2.20] showed to suppress the thermal striations due to temperature oscillation and also to reduce the oxygen density by imposing a transverse magnetic field, experiments on the magnetic Czochralski method have been extensively carried out to understand the effects of magnetic fields on the melt [2.19]-[2.23].

Before summarizing the recent research in the magnetic Czochralski method, let us review the effects of a magnetic field on the melt qualitatively.

Effects of an external magnetic field on the melt differ depending on the direction of the magnetic field. If a magnetic field is imposed, the Lorentz force $\vec{F}$ given by the following equation would be applied to the melt

$$\vec{F} = \vec{J} \times \vec{B} \ , \qquad (2.2.8)$$

where $\vec{J}$ is the current density vector and $\vec{B}$ is the magnetic field flux density vector.

Variables $\vec{J}$ and $\vec{B}$ must satisfy Maxwell's equations, but in order to simplify the problem, let us concentrate only on the term influenced by the magnetic field. Taking this point into account, the Lorentz force can be approximated as

$$\vec{F} = \sigma_e \left(\vec{u} \times \vec{B}\right) \times \vec{B} \ , \qquad (2.2.9)$$

where σ_e is the electric conductivity and $\vec{u}$ is the melt velocity. In this derivation, the Ohm's law is used

$$\vec{J} = \sigma_e \vec{u} \times \vec{B} \ . \qquad (2.2.10)$$

As expressed in Eq.(2.2.9), the Lorentz force works in the perpendicular direction to the melt to reduce the fluid velocity.

Common ways to impose a magnetic field have been either in the vertical direction or in the transverse direction [2.19]-[2.21]. Fig. 2.2.1 describes the schematic illustration about the relationship between the direction of an external magnetic field and the convective flows. For the transverse direction, the z-direction velocity is suppressed as the dashed arrows in Fig.2.2.1 a) shows. The suppression of ascending and descending convective flows prevents impurities form migrating from the melt into the crystal while the axisymmetric flow and temperature are disturbed, which causes oscillation on the crystal melt interface. On the other hand, a magnetic field in the vertical direction suppresses the radial and circumferential directions. Therefore, the axisymmetric profiles of the flow and the temperature can be maintained, but the impurity density tends to increase since the stagnant layer is formed near the free surface.

Recently, the cusp magnetic field configuration has been proposed for purpose of combining the advantages of both the transverse and the vertical magnetic field configurations [2.9],[2.22],[2.23]. According to the experiments conducted by Hirata [2.22] for a three-inch diameter silicon crystal, efficient control of the dopant and oxygen densities was materialized.

The attention toward numerical analyses in the magnetic Czochralski methods has increased associated with the advancement in the computer technology and the computational technique. First of all, a theoretical analysis was conducted by Kobayashi

to examine the effects of an external magnetic field on the Czochralski crystal growth [2.24]. The series expansion analysis was applied to forced convection due to rotation of the crystal in cases of both an axial and a transverse magnetic fields. As a result, the axial magnetic field proved more effective to suppress forced convection than the transverse field did.

Magnetohydrodynamic flows in an enclosure are analyzed in the presence of a lateral magnetic field and the effects of the Hartmann number and the magnetic Prandtl number were studied [2.25]. Munakata, et al. also computed two-dimensional melt flows in both the Bridgman and the Czochralski growth processes by imposing an external vertical magnetic field [2.26]. The analysis estimated the minimum intensity of the magnetic field to suppress natural convective flows and showed that the velocity field could be reduced inversely proportional to the square of the magnetic field.

The numerical analyses have been extended to the axisymmetric simulations [2.5], [2.21], [2.27]-[2.29] as well as the three-dimensional ones[2.6], [2.9], [2.29]. Ozoe, et al. studied the effects of axial magnetic field on the axisymmetric flow in a Czochralski crucible by varying the Hartmann number [2.27]. They also computed the three-dimensional natural convection in a cubical enclosure with various direction of external magnetic fields and reported that the magnetic field parallel to the heated wall was not sufficient to suppress the natural convective flows [2.30]. Munakata and Tanahashi conducted both numerical and experimental studies to investigate parameter sensitivity and the effects of the magnetic field on the induction of oscillatory flows [2.28]. Series [2.21] and Riley [2.29] focused on the species transport and distribution in the cylindrical coordinate system.

For three-dimensional Czochralski melt analyses, Milecic and Wingerath [2.6] computed the Czochralski melt flow with axisymmetric temperature boundary conditions on the crucible wall in the presence of an axial magnetic field and observed the effects of the magnetic field on the temperature oscillation and time periodic flow.

Although most of the previous numerical analyses in the magnetic Czochralski melt flow concentrated on either axial or transverse magnetic field, the Czochralski melt flow in the cusp magnetic field configuration has been done by Hirata [2.9]. The analysis was

simulated by the finite difference method in the unsteady state and the three-dimensions using the governing equation of the magnetic field in stead of the electric potential.

The most crucial issue for the numerical analysis in the magnetic Czochralski method is the large number of variables, for example, six variables ($\vec{u} = (u_x, u_y, u_z)$, P, T, and ϕ) in case of using the electric potential and eleven variables ($\vec{u} = (u_x, u_y, u_z)$, P, T, $\vec{B} = (B_x, B_y, B_z)$, and $\vec{J} = (J_x, J_y, J_z)$) in case of using a magnetic field. Therefore, it is quite important to develop an effective numerical algorithm with respect to memory and CPU time requirements, particularly, for transient three-dimensional problems. The other issue is the lack of experimental data to compare the numerical results due to the difficulty in measuring the velocity, the temperature and the magnetic field.

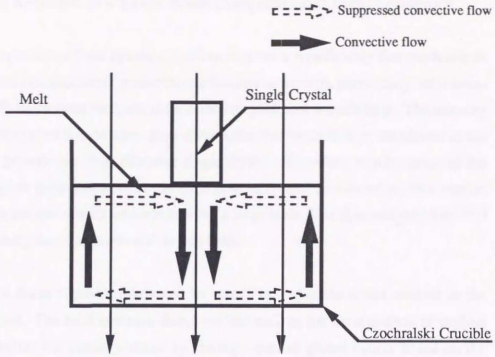

a) A magnetic field in the vertical direction

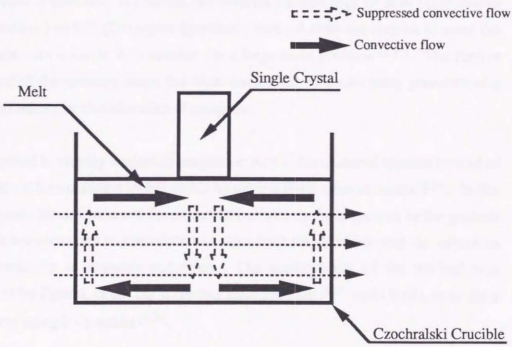

b) A magnetic field in the transverse direction

Fig. 2.2.1 Schematic illustration of relationship between the direction of an imposing magnetic feild and convective flows

2.3 Recent Research in a Large Scale Computational Fluid Dynamics

Since the computational fluid dynamic problem requires a significantly fine mesh size in order to prevent introduction of numerical oscillations and errors, particularly for a three-dimensional finite element analysis, the memory requirement is quite large. The memory requirement is expected to become quite demanding for the melt flow simulation in the Czochralski growth of a large diameter single crystal. Therefore, minimization of the memory usage is quite essential in the melt flow analysis. In this sense, this section focuses on the computational methods to solve a large scale fluid dynamic problem [2.31] and review briefly the current research in this field.

In general, the finite element matrix can be solved by either the direct method or the iterative method. The most common direct method such as the band method or skyline method minimizes the memory usage by storing a part of global matrix based on the characteristics of the matrix [2.32]. However, despite the reduction in memory requirement, the direct method can not be applied to a large scale problem with more than 10,000 degrees of freedom. In contrast, the iterative method such as SOR (Successive Over Relaxation) or CG (Conjugate Gradient) method does not require to store the global matrix. As a result, it is suitable for a large scale problem [2.33]. The further improvement of the memory usage has been carried out by considering geometry of a finite element matrix or characteristics of computer.

Gresho proposed to employ numerical integration only at the center of element instead of at eight nodes in formulating a global matrix by using a finite element matrix [2.34]. In this method, because the diffusion and the advection matrices can be expressed by the gradient matrix, it is not necessary to formulate and store both the diffusion and the advection matrices, resulting in memory reduction. The applicability of the method was demonstrated by Eguchi, et al. for a laminar fluid problem [2.35] and Okuda, et al. for a turbulent flow using $k - \varepsilon$ model [2.31].

Associated with recent advancement in super computer and parallel computer technologies, the numerical algorithm has been developed by taking advantage of the computer characteristics. One of the most effective ways is to divide an analysis region

into a number of sub-regions. Since the analysis in each sub-region can be performed separately without formulating a large size global matrix, it can reduce the memory size.

In these methods based on division of an analysis region, the values of the shared boundaries have to be assigned somehow in order to analyze each sub-region individually. There are mainly two methods in determining the shared boundary values: 1) the domain decomposition method [2.31],[2.36],[2.37], and 2) the substructure method [2.38]-[2.40]. The domain decomposition method determines the values of the shared boundary condition in an iterative way while the substructure method determines in a direct way. The details of both methods are explained in Chapter 4.

[References]

[2. 1] Sackinger, P. A., Brown, R. A., and Derby, J. J.," A Finite Element Method for Analysis of Fluid Flow, Heat Transfer and Free Interfaces in Czochralski Crystal Growth", International Journal For Numerical Methods in Fluids, Vol.9, pp.453-492(1989).

[2. 2] Brown, R. A., Kinney, T. A., Sackinger, P.A., and Bornside, D. E., " Toward an Integrated Analysis of Czochralski Growth", Journal of Crystal Growth, Vol.97, pp.99-115(1989).

[2. 3] Tsukada, T., Imishi, N. and Hozawa, M., " Theoretical Study of the Flow and Temperature Fields in CZ Single Crystal Growth", Journal of Chemical Engineering of Japan, Vol.21, pp.184-191(1988).

[2. 4] Tsukada, T., Imishi, N. and Hozawa, M., " Effect of a Radiation Shield on Melt/Crystal Interface Shape and Pull Rate of Silicon CZ Puller", Journal of Chemical Engineering of Japan, Vol.21, pp.381-387(1988).

[2. 5] Langlois, W., and Lee, H. J., " Czochralski Crystal Growth in an axial Magnetic Field: Effects of Joule Heating", Journal of Crystal Growth, Vol.62, pp.481-486(1983).

[2. 6] Mihelcic, M., and Wingerath, K. " Numerical Simulations of the Czochralski Bulk Flow in an axial Magnetic Field: Effects on the Flow and Temperature Oscillations in the Melt", Journal of Crystal Growth, Vol.71, pp.163-168(1985).

[2. 7] Ikuo, S., Tanaka, M., and Nakamura, M., " Numerical Analysis of Thermal Convection in Si Melt During Growth of a Single Crystal" (in Japanese), Yawata Technical Report, Vol.330, pp.37-43(1988).

[2. 8] Cartwright, R., Ilegbusi, O. J., and Szekely, J., " A Comparison of Order-of-

Magnitude and Numerical Analyses of Flow Phenomena in Czochralski and Magnetic Czochralski Systems", Journal of Crystal Growth, Vol.94, pp.321-333(1989).

[2. 9] Hirata, H.,Ph.D Thesis, The University of Tokyo, Department of Elctrical Engineering (in Japanese)(1991).

[2. 10] Kakimoto, K., Eguchi, M., et al.," Natural And Forced Convection of Molten Silicon During Czochralski Single Crystal Growth", Journal of Crystal Growth, Vol. 94, pp.412-420(1989).

[2. 11] Imaishi, N. and Housawa, M., " Fluid Mechanics and Heat Transfer in Single Crystal Production"(in Japanese), Kagaku Kougyo, Vol.52, pp.803-807(1988).

[2. 12] Derby, J. J., Brown, R. A., et al., " Finite Element Analysis of a Thermal-Capillary model for Liquid Encapsulated Czochralski Growth", Journal of Electrochemistry Society: Solid-State Science and Technology,Vol.132, pp.470-482(1985).

[2. 13] Atherton, L. J., Derby, J. J., and Brown, R. A., " Radiative Heat Exchange in Czochralski Crystal Growth", Journal of Crystal Growth, Vol.84, pp.57-78(1987).

[2. 14] Dupret, F., Nicodeme, P., et al., " Global Modeling of Heat Transfer in Crystal Growth Furnaces", International Journal of Heat and Mass Transfer, Vol.33., pp.1849-1871(1990).

[2.15] Kiney, T. A., Bornside, D. E., et al.., " Quantitative Assessment of an Integrated Hydrodynamic Thermal-Capillary Model for large-Diameter Czochralski Growth of Silicon: Comparison of Predicted temperature Field with Experiment", to be published in Journal of Crystal Growth.

[2. 16] Kobayashi, N., " Heat transfer in Czochralski Crystal-Growth Melts",

Preparation and Properties of Solid State Materials , Vol.6, Marcel Dekker, New York, pp.119-253(1981).

[2. 17] Langlois, W. E., " Buoyancy-Driven Flows in Crystal-Growth Melts", Annual Review Fluid Mechanics, Vol.17, pp.191-215(1985).

[2. 18] Mihelcic, M., Wingerath, K., and Pirron, C., " Three-Dimensional Simulations of the Czochralski Bulk Flow", Journal of Crystal Growth, Vol.69, pp.473-488(1984).

[2. 19] Hoshikawa, K., and Hirata, H., " Growth of Single Crystals in the Presence of a Magnetic Field", Nihon Kesshou- Gakkai-Shi (in Japanese), Vol.27, pp.177-188(1985).

[2. 20] Hoshi, K., Suzuki, N., Okubo, T., and Isawa, N., Extended Abstracts of Electrochemistry Society, Spring Meeting, pp.811-813(1980).

[2. 21] Series, R. W., " Czochralski Growth of Silicon Under an Axial Magnetic Field", Journal of Crystal Growth, Vol.97, pp.85-91(1989).

[2. 22] Hirata, H., and Hoshikawa, K., " Silicon Crystal Growth in a Cusp Magnetic Field", Journal of Crystal Growth, Vol.96, pp.747-755(1989).

[2. 23] Hirata, H., and Hoshikawa, K., " Homogeneous Increase in Oxygen Concentration in Czochralski Silicon Crystal by a Cusp Magnetic Field", Journal of Crystal Growth, Vol.98, pp.777-786(1989).

[2. 24] Kobayashi, S., " Effects of an External Magnetic Field on Solute Distribution in Czochralski Grown Crystals - A Theoretical Analysis", Journal of Crystal Growth, Vol.75, pp.301-308(1986).

[2. 25] Ozoe, H., Maruo, E., and Matsuo, H., " Numerical Analyses of Transient Natural Convection of Liquid Metals After a Step Change in an External Lateral

Magnetic Field"(in Japanese), Kagaku Kogaku Ronbunshu, Vol.16, pp.990-997(1990)

[2. 26] Munakata, T., and Tanasawa, I., " The effect of an external Magnetic Field on Natural Convection During the Crystal Growth Process from a Melt", Transactions of the Japan Society of Mechanical Engineers, B-Vol.51, pp.2545-2549(1988).

[2. 27] Ozoe, H., and Toh, K., " Numerical Computation For a Czochralski Bulk Flow of Liquid Metals Under a Vertical External Magnetic Field", Proceedings of 9th International Heat Transfer Conference, Jerusalem, Vol.6, pp.311-316(1990).

[2. 28] Munakata, T., and Tanasawa, I., " A study of the Onset of Oscillatory Flow in a Czochralski Growth Melt and Its suppression by a Magnetic Field", Transactions of the Japan Society of Mechanical Engineers, B-Vol. 55, pp.2610-2617(1989).

[2. 29] Riley, N., " Species Transport in Magnetic Field Czochralski Growth", Journal of Crystal growth, Vol.97,pp.85-91(1989).

[2. 30] Ozoe, H., and Okada, K., " The Effect of the Direction of the External Magnetic Field on the Three-Dimensional Convection in a Cubical Enclosure", International Journal of Heat and Mass transfer, Vol.32, pp.1939-1954(1989).

[2. 31] Okuda, H., Ph.D Thesis, The University of Tokyo, Department of Nuclear Engineering (in Japanese) (1989).

[2.32] Bathe, K. J., Finite Element Procedures in Engineering Analysis, Prentice-Hall, Inc., Englewood Cliffs, N. J., U.S.A.(1982).

[2.33] Murata, T., Oguni, C., and Karaki, S., Super Computer: Application to Scientific Simulations (in Japanese), Maruzen Publisher, Tokyo, Japan(1985).

[2. 34] Gresho, P. M., et al., " A modified Finite Element Method for Solving the

Time-Dependent, Incompressible Navier–Stokes Equations. Part 1 : Theory", International Journal of Numerical Methods in Fluids, Vol.4, pp.557-598(1984).

[2. 35] Eguchi, Y., and Yagawa, G., " Thermal Hydraulic Analysis of Flows in the Upper Plenum of Fast Breeder Reactor"(in Japanese), Journal of the Atomic Energy Society of Japan, Vol.30, pp.78-86(1988).

[2. 36] Glowinski, R., et al., " Domain Decomposition Methods For Nonlinear Problems in Fluid Dynamics", Computational Mechanics In Applied Mechanics and Engineering, Vol.40, pp.27-109(1983)

[2. 37] Yuasa, A., Okuda, H., and Yagawa, G., " Efficiency of Domain Decomposition Technique for Incompressible Viscous Flow Analysis"(in Japanese), Proceedings of JSME 67th conference, No.900-14, Vol.A, pp.517-519(1990).

[2. 38] Carter, W. T. Jr., Sham, T. L., and Kincho, H. L., " A Parallel Finite Element Method and Its Prototype Implementation on a HyperCube", Computers & Structures, Vol. 31, pp.921-934(1989).

[2.39] Sheu, C. H., De Roeck, G., Van Laethem, M., and Geyskens, P., " Application of the Substructuring Technique to Non-linear Dynamic Structural Analysis", Computers & Structures, Vol. 35 , pp.593-601(1990).

[2. 40] El-Sayed, M. E. M., and Hsiung, C. K., " Parallel Finite Element Computation with Separate Substructres", Computers & Structures, Vol.36, pp.261-265(1990).

Chapter 3

Theory and Numerical Analysis Model for Melt Flows

3.1 Introduction

The melt flow during growth of a single crystal consists of complex transient physical phenomena in three-dimensions. In particular, when a magnetic field is imposed on the melt flow to control the convective flows, the melt flow analysis has to consider not only fluid and thermal effects but also electromagnetic effects, namely has to solve a magneto-thermal-hydraulic problem. An analysis of a magneto-hydro-dynamic flow requires to solve coupled physical behavior in which velocity, temperature and magnetic field interact one another. Therefore, the governing equations of a magneto-thermal-hydrodynamic flow consists of equations which represent each physical motions in the three fields: flow, thermal and magnetic fields.

In this chapter, the derivation of governing equation of a magneto-thermal-hydraulic flow is described. Particularly, the derivation of an electric potential equation is discussed in detail, including assumptions. After the boundary conditions are identified, the space discretization by finite element method is presented. Since the MAC (Marker And Cell) method is used for the time integration scheme, the derivations of the pressure Poisson equation and the velocity field equation are described based on the MAC method. Finally, the resulting governing equations are summarized in the form of the finite element matrices.

3.2 Governing Equations of Magneto-Thermal-Hydraulic Flows

First of all, the continuity (incompressible condition) and Navier-Stokes equations used

for a flow field are as follows:

$$\vec{\nabla}\cdot\vec{u}=0 \quad , \tag{3.2.1}$$

$$\frac{\partial\vec{u}}{\partial t}+\vec{u}\cdot\vec{\nabla}\vec{u}=-\frac{1}{\rho}\vec{\nabla}P+\nu\nabla^2\vec{u}+\vec{F_b} \quad , \tag{3.2.2}$$

where $\vec{u}$ is the velocity vector ($\vec{u}=(u_x,u_y,u_z)$ for three-dimensions), P is the pressure, and $\vec{F_b}$ is the body force vector. The symbol ρ denotes the density of fluid, and ν denotes the dynamic viscosity.

The flow caused by natural convection or magnetohydrodynamic forces is taken into account in the third term of the right hand side in Eq.(3.2.2) as the external body force. Therefore, for a magneto-thermal-hydraulic flow, the vector $\vec{F_b}$ is given by using Boussinesq approximation and the Lorentz force:

$$\vec{F_b}=-\beta\vec{g}(T-T_b)+\frac{1}{\rho}\vec{J}\times\vec{B} \quad , \tag{3.2.3}$$

where the variables T, T_b, $\vec{g}$, $\vec{J}$ and $\vec{B}$ are the actual temperature of the fluid, the averaged temperature of the fluid, the gravity vector, the current density vector and the magnetic flux density vector, respectively. The symbol β denotes the coefficient of volumetric expansion. The expression for the Lorentz force $\left(\vec{J}\times\vec{B}\right)$ can be simplified by using magnetohydrodynamic (MHD) approximation. The details will be explained later in this section.

Secondly, the governing equation for a thermal field is given by

$$\frac{\partial T}{\partial t}=-\vec{\nabla}\cdot(\vec{u}\,T)+\alpha\,\nabla^2T \quad , \tag{3.2.4}$$

where α is the coefficient of thermal diffusivity.

While the forced convective flow is obtained by solving Navier-Stokes equation (3.2.2)

and energy equation (3.2.4) separately, the natural convection flow requires solving the coupled equations of Eqs.(3.2.2) and (3.2.4) .

Finally, the equation for a magnetic field can be derived from Maxwell equations (3.2.5) – (3.2.8) and Ohm's law (3.2.9) by using magnetohydrodynamic approximation. Maxwell equations are given by

$$\vec{\nabla} \times \vec{E} = -\frac{\partial \vec{B}}{\partial t} , \tag{3.2.5}$$

$$\vec{\nabla} \times \vec{B} - \mu_e \frac{\partial \vec{D}}{\partial t} = \mu_e \vec{J} , \tag{3.2.6}$$

$$\vec{\nabla} \cdot \vec{D} = \rho_o , \tag{3.2.7}$$

$$\vec{\nabla} \cdot \vec{B} = 0 , \tag{3.2.8}$$

$$\vec{J} = \rho_o \vec{u} + \sigma_e (\vec{E} + \vec{u} \times \vec{B}) , \tag{3.2.9}$$

where $\vec{E}$ and $\vec{D}$ are electric field intensity and electric displacement, respectively. The physical parameter ρ_o is the electric charge density of a fluid, μ_e is the magnetic permeability, and σ_e is the electrical conductivity.

In deriving the mathematical model for the electromagnetic force, the equations are simplified based on the following assumptions [3.1],[3.2].

1. The displacement current is assumed to be zero ($\frac{\partial \vec{D}}{\partial t} = 0$).
2. The effect of variations in the charge density is negligible.
3. In Czochralski Growth of silicon, the magnetic Reynolds number ($R_m = \mu_e \sigma_e L V$) is small enough that the internally induced magnetic field can be neglected compared with the externally imposed magnetic field B_o.

Based on the assumptions, Eqs. (3.2.5) and (3.2.6) can be rewritten in the quasi-static form of Maxwell's equations as

$$\vec{\nabla} \times \vec{E} \approx 0 \ , \qquad (3.2.5)'$$

$$\vec{\nabla} \times \vec{B} = \mu_e \vec{J} \ , \qquad (3.2.6)'$$

Due to the condition given by Eq.(3.2.5)', electric field can be expressed by introducing the electric scalar potential as follows:

$$\vec{E} = -\vec{\nabla}\phi \ , \qquad (3.2.10)$$

where the vector identity $\vec{\nabla} \times \left(-\vec{\nabla}\phi\right) = 0$ is used in deriving Eq.(3.2.10).

Substituting Eq. (3.1.10) into Eq. (3.2.9), Ohm's law can be rewritten as

$$\vec{J} = \sigma_e \left(-\vec{\nabla}\phi + \vec{u} \times \vec{B} \right) \ . \qquad (3.2.11)$$

Furthermore, the continuity condition for electric current is required:

$$\vec{\nabla} \cdot \vec{J} = 0 \ . \qquad (3.2.12)$$

Therefore, Eqs. (3.2.11) and (3.2.12) lead to the equation for unknown electric scalar potential ϕ:

$$\nabla^2 \phi = \vec{\nabla} \cdot (\vec{u} \times \vec{B}) \qquad (3.2.13)$$

As a result, the governing equations for magnetic-thermal-hydraulic flows are summarized as follows:

$$\vec{\nabla} \cdot \vec{u} = 0 \qquad (3.2.14)$$

$$\frac{\partial \vec{u}}{\partial t} + \vec{u} \cdot \vec{\nabla}\vec{u} = -\frac{1}{\rho}\vec{\nabla}P + \nu\nabla^2\vec{u}$$

$$- \beta\vec{g}(T - T_s) + \frac{\sigma_e}{\rho}\left(-\vec{\nabla}\phi + \vec{u} \times \vec{B} \right) \times \vec{B} \qquad (3.2.15)$$

$$\frac{\partial T}{\partial t} = -\vec{\nabla}\cdot(\vec{u}T) + \kappa\nabla^2 T \tag{3.2.16}$$

$$\nabla^2\phi = \vec{\nabla}\cdot(\vec{u}\times\vec{B}) \tag{3.2.17}$$

3.3 Boundary Conditions of Magneto-Thermal-Hydraulic Flows

The governing equations (3.2.15) – (3.2.17) for magneto-thermal-hydraulic flows are solved under boundary conditions of either the Dirichlet type or the Neumann type.

The Dirchlet type of boundary conditions for each variable is defined as:

velocity: $\vec{u} = \hat{\vec{u}}$,

temperature: $T = \hat{T}$, on Γ_d (3.3.1)

electric potential: $\phi = \hat{\phi}$,

where Γ_d denotes the boundary which the Dirchlet type is assigned, and $\widehat{()}$ denotes the given value of the boundary condition.

On the other hand, the Neumann type of boundary condition for each variable on the boundary Γ_n are defined as:

traction force: $\vec{\tau} = \hat{\vec{\tau}}$,

heat flux: $\vec{q} = \hat{\vec{q}}$, on Γ_n (3.3.2)

gradient of electric potential: $\frac{\partial\phi}{\partial n} = \widehat{\frac{\partial\phi}{\partial n}}$,

The i direction of the traction force $\vec{\tau}$ is given by

$$\tau_i = \left\{ -\frac{1}{\rho} P \, \delta_{ij} + \nu \, u_{i,j} \right\} n_j \ , \tag{3.3.3}$$

where δ_{ij} is Kronecker's delta, and n_i is the unit vector normal to the boundary Γ_n. The subscripts i and j take 1 or 2 for two-dimensional analysis and take from 1 to 3 for three-dimensional analysis.

3.4 Finite Element Discretization of Magnet-Thermal-Hydrodynamic Equations

The Governing Eqs.(3.2.14) – (3.2.17) are reduced to a set of residual equations by the method of weighted residuals [3.3]. The partial integration is carried out for the pressure gradient term and diffusion term in Navier-Stokes Eq.(3.2.15), the diffusion term in energy Eq.(3.2.16), and the Laplacian in the electric potential Eq.(3.2.17).

After obtaining a set of residual equations, the velocity, the temperature and the electric potential are discretized in space using a mixed finite element basis function and Galerkin's method. Eight-node solid elements are used for finite element mesh division. Thus, the velocity, the temperature and electric potential are approximated by bilinear basis functions (Φ_α) while pressures is approximated by piecewise constant value (ψ_e) as follows[3.4]:

$$u_i = \sum_{\alpha=1}^{N_n} u_{i\alpha} \Phi_\alpha \ , \tag{3.4.1}$$

$$P = \sum_{e=1}^{N_e} P_e \psi_e \ , \tag{3.4.2}$$

$$T = \sum_{\alpha=1}^{N_n} T_\alpha \Phi_\alpha \ , \tag{3.4.3}$$

$$\phi = \sum_{\alpha=1}^{N_n} \phi_\alpha \Phi_\alpha \ , \tag{3.4.4}$$

where N_n and N_e are the total number of nodes and elements, respectively. The subscript i takes from 1 to 3 corresponding to x-, y- and z- direction in the three-dimensions.

Therefore, the finite element matrix equations for magneto-thermal-hydrodynamic equations are written as follows:

$$\boldsymbol{C}^t \mathrm{u} = 0 \ , \tag{3.4.5}$$

$$\boldsymbol{M}\ \dot{\mathrm{u}} + \boldsymbol{B}(\mathrm{u})\ \mathrm{u} - \boldsymbol{C}\ \mathrm{P} + \boldsymbol{D}_{\boldsymbol{u}}\mathrm{u} = \boldsymbol{f}_{\boldsymbol{u}} \ , \tag{3.4.6}$$

$$\boldsymbol{M}\ \dot{\mathrm{T}} + \boldsymbol{B}(\mathrm{u})\ \mathrm{T} + \boldsymbol{D}_{\boldsymbol{T}}\ \mathrm{T} = \boldsymbol{f}_{\boldsymbol{T}} \ , \tag{3.4.7}$$

$$\boldsymbol{D}_{\phi}\ \phi + \boldsymbol{C}_{\phi}^{t}\ \mathrm{ub} = \boldsymbol{f}_{\phi} \ . \tag{3.4.8}$$

Here, u ,T, b and ϕ are nodal vectors for the velocity, the temperature, the magnetic field and the electric potential, respectively. The variable P is the vector of pressure in elements, and $\boldsymbol{f}_{\boldsymbol{u}}, \boldsymbol{f}_{\boldsymbol{T}}$, and $\boldsymbol{f}_{\phi}$ are the vector corresponding to external forces in the velocity, temperature and magnetic fields. The coefficient matrices $\boldsymbol{B}(\mathrm{u})$, $\boldsymbol{C}$, $\boldsymbol{C}_{\phi}$, $\boldsymbol{D}$, $\boldsymbol{D}_{\phi}$, and $\boldsymbol{M}$ in Eqs.(3.4.5) – (3.4.8) are the advection, the gradient for the velcoty field, the gradient for the magetic field, the diffusion for the velocity, the diffusion for the magnetic field and mass terms defined as follows:

$$M^{\alpha\beta} = \int_{\Omega} \Phi_{\alpha}\Phi_{\beta}\, d\Omega \ , \tag{3.4.9}$$

$$C^{\alpha i} = \int_{\Omega} \frac{\partial \Phi_{\alpha}}{\partial x_i}\psi_e\, d\Omega \ , \tag{3.4.10}$$

$$B^{\alpha\beta} = \int_{\Omega} \Phi_{\alpha}\left(\Phi_{\gamma}u_{j\gamma}\right)\frac{\partial \Phi_{\beta}}{\partial x_j}\, d\Omega \ , \tag{3.4.11}$$

$$D_{u}^{\alpha\beta} = \int_{\Omega} \nu \frac{\partial \Phi_{\alpha}}{\partial x_j} \cdot \frac{\partial \Phi_{\beta}}{\partial x_j}\, d\Omega \ , \tag{3.4.12}$$

$$D_T^{\alpha\beta} = \int_\Omega \alpha \frac{\partial \Phi_\alpha}{\partial x_j} \cdot \frac{\partial \Phi_\beta}{\partial x_j} d\Omega \ , \tag{3.4.13}$$

$$D_\phi^{\alpha\beta} = \int_\Omega \frac{\partial \Phi_\alpha}{\partial x_j} \cdot \frac{\partial \Phi_\beta}{\partial x_j} d\Omega \ , \tag{3.4.14}$$

$$C_\phi^{\alpha i} = \int_\Omega \frac{\partial \Phi_\alpha}{\partial x_i} \Phi_\alpha \, d\Omega \ . \tag{3.4.15}$$

For numerical integration, the eight point of Gauss-Legendre integration (2 x 2 x 2) is used.

3.5 Time Integration Scheme

For time integration scheme, the MAC Method [3.5],[3.6] is used. In this method, the incompressible condition is incorporated with time integration by splitting a velocity and a pressure.

In the MAC method, both a velocity and a pressure is discretized explicitly in time. Therefore, Eqs.(3.4.5) and (3.4.6) are written as

$$\boldsymbol{C}^t \, u^{n+1} = 0 \ , \tag{3.5.1}$$

$$u^{n+1} = u^n + \Delta t \, \boldsymbol{M}^{-1}\left[\boldsymbol{C} P^{n+1} - (\boldsymbol{B}(\boldsymbol{u}) u^n + \boldsymbol{D}_{\boldsymbol{u}} u^n) + \boldsymbol{f}_{\boldsymbol{u}}{}^n\right] \ . \tag{3.5.2}$$

At time step n+1, the continuity equation (3.5.1) is assumed to be satisfied. Therefore, a pressure at time step n can be obtained by solving the following equation.

$$\boldsymbol{C}^t \boldsymbol{M}^{-1} \boldsymbol{C} \, P^{n+1} = -\frac{1}{\Delta t} \boldsymbol{C}^t u^n + \boldsymbol{C}^t \boldsymbol{M}^{-1}\left(\boldsymbol{B}(\boldsymbol{u}) u^n + \boldsymbol{D}_{\boldsymbol{u}} u^n - \boldsymbol{f}_{\boldsymbol{u}}{}^n\right) \ , \tag{3.5.3}$$

After a pressure P^{n+1} is obtained, velocity u^{n+1} can be given by Euler time integration in Eq. (3.5.2).

3.6 Summary of Governing Equations for Magneto-Thermal-Hydraulic Flows

Finite element matrix equations using the MAC time integration scheme is summarized as follows:

$$\boldsymbol{C}^t\boldsymbol{M}^{-1}\boldsymbol{C}\,\mathrm{P}^{n+1} = -\frac{1}{\Delta t}\boldsymbol{C}^t\mathrm{u}^n + \boldsymbol{C}^t\boldsymbol{M}^{-1}\left(\boldsymbol{B}(\boldsymbol{u})\mathrm{u}^n + \boldsymbol{D}_u\mathrm{u}^n - \boldsymbol{f}_u{}^n\right) \tag{3.6.1}$$

$$\boldsymbol{D}_\phi\phi^n = -\boldsymbol{C}_\phi^t\,\mathrm{u}^n\mathrm{b} + \boldsymbol{f}_\phi^n \tag{3.6.2}$$

$$\mathrm{u}^{n+1} = \mathrm{u}^n + \Delta t\,\boldsymbol{M}^{-1}\left[\boldsymbol{C}\mathrm{P}^{n+1} - (\boldsymbol{B}(\boldsymbol{u})\mathrm{u}^n + \boldsymbol{D}_u\mathrm{u}^n) + \boldsymbol{f}_u{}^n\right] \tag{3.6.3}$$

$$\mathrm{T}^{n+1} = \mathrm{T}^n + \Delta t\,\boldsymbol{M}^{-1}\left[-(\boldsymbol{B}(\boldsymbol{u})\mathrm{T}^n + \boldsymbol{D}_T\mathrm{T}^n) + \boldsymbol{f}_T{}^n\right] \tag{3.6.4}$$

The schematic flow chart which describes the procedure of solving Eqs. (3 6.1) – (3.6.4) is shown in Fig.3.6.1.

The matrix $\boldsymbol{C}^t\boldsymbol{M}^{-1}\boldsymbol{C}$ is the Laplacian in discretized from by the finite element method. Eq.(3.6.1) is the Poisson equation as well as Eq.(3.6.2). Memory size and CPU time required to solve Eqs.(3.6.3) and (3.6.4) are not so demanding as those to solve Eqs.(3.6.1) and (3.6.2) because explicit method leads to a simple substitution calculation. On the contrary, Eqs. (3.6.1) and (3.6.2) require to solve finite element matrices. The solver for these Poisson equations will be discussed in the following chapter.

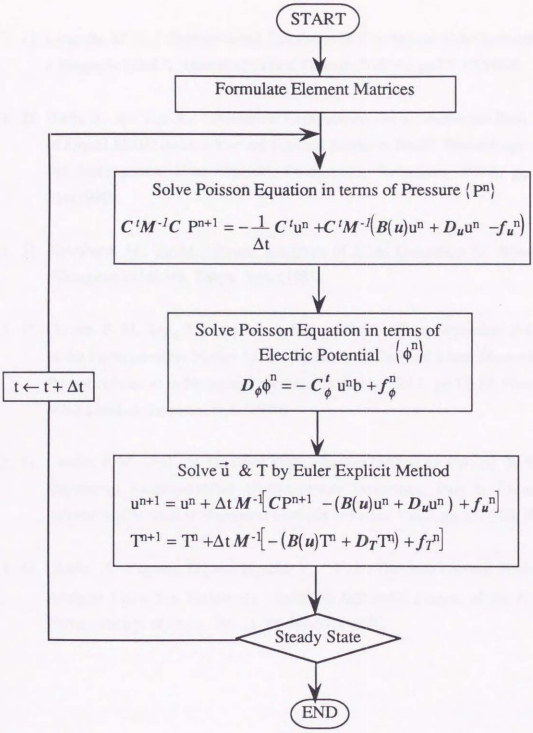

Fig.3.6.1 Flow chart for magneto-thermal-hydraulic flow analysis using the MAC method

[References]

[3. 1] Langolis, W. E., " Computational Simulation of Czochralski Melt Convection in a Magnetic Filed ", Journal of Crystal Growth, Vol.70., pp.73-77(1984).

[3. 2] Ozoe, H., and Toh, K., " Numerical Computation For a Czochralski Bulk Flow of Liquid Metals under a Vertical External Magnetic Field", Proceedings of the 9th International Heat Transfer Conference, Jerusalem, Vol.6, pp.311-316(1990).

[3. 3] Kawahara, M., Finite Element Analyses of Fluid Dynamics (in Japanese), Nikkagiren Publisher, Tokyo, Japan(1985).

[3. 4] Gresho, P. M., Lee, R. L., and Sani, R. L., " On the Time-Dependent Solution of the Incompressible Navier-Stokes Equations in Two and Three Dimensions", Recent Advances in Numerical Methods in Fluids, Vol.1, pp.27-79, Pineridge Press Limited, Swansea, U.K.(1980).

[3. 5] Gresho, P. M., et al.," A Modified Finite Element Method for Solving the Time-Dependent Incompressible Navier-Stokes Equations, Part I; Theory ", International Journal of Numerical Methods in Fluids, Vol.4, pp.557-598(1984).

[3. 6] Okuda, H., Yagawa, G., and Eguchi, Y., " Finite Element Thermal Hydraulic Analysis Using k–ε Turbulence Model"(in Japanese), Journal of the Atomic Energy Society of Japan, Vol.31, pp.588-598(1989).

Chapter 4

Implementation of the Substructure Method to Melt Flows

4.1 Introduction

The most common numerical method used to solve an incompressible flow problem is to incorporate the incompressible condition expressed as the continuity equation with the Navier-Stokes equation by separating a velocity and a pressure formulated on either explicit or implicit time integration schemes such as the MAC or the fractional step method. Such time integration schemes would result in derivation of the Poisson equation for a pressure. In solving an incompressible flow, the most demanding calculations in terms of memory requirement and CPU time is in solving the Poisson equation.

The global matrix of the Poisson equation is symmetric-positive-definite matrix [4.1]. Although various types of numerical algorithms have been considered, the most appropriate solver for the Poisson equation depends on the problem. For an analysis of the Czochralski melt, since geometry of the Czochralski crucible is axisymmetric, the analysis region can be divided into identical sub-regions as illustrated in Fig. 4.1.1 in the case of four divisions. Once the partitioned stiffness matrix ABCDEF is formed, it can be used for the remaining three substructure stiffness matrices. This would allow to minimize memory storage and CPU time.

In this chapter, two types of solvers for the Poisson equation are presented. One is the conjugate gradient method, which is one of the most practical iterative methods for a sparse symmetric-positive-definite matrix [4.2],[4.3]. The conjugate gradient method can be used without storing a global matrix. While this method does not require a large amount of memory size, CPU time could become quite high, particularly for a large scale

transient problem since a global matrix is formulated for every iteration of the conjugate gradient method at every time step. Therefore, an alternative method is necessary to be developed which can adequately operate within the requirements for both memory size and CPU time. In this sense, a substructure method is proposed by taking advantage of the characteristics of Czochralski crucible geometry. The characteristics of substructure method is summarized, as opposed to domain decomposition methods, which is another analysis method that splits an analysis region into a number of sub-domains. .Advantages and disadvantages of each method are discussed referring to differences between two methods.

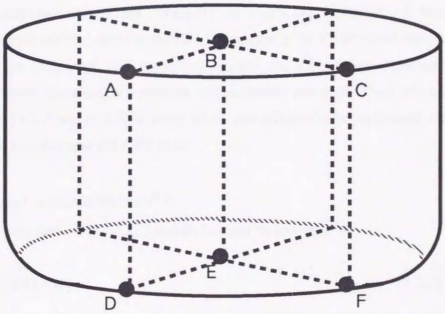

Fig.4.1.1 Division of an analysis region into four substurctures for the substructure method applied to melt flows during the Czochralski crystal growth

4.2 Solver for the Poisson Equation

4.2.1 Characteristics of the Poisson Equation

Let us restate the governing equations for a magneto-thermal-hydraulic flow based on the MAC method:

$$\boldsymbol{C}^t\boldsymbol{M}^{-1}\boldsymbol{C}\,\mathrm{P}^{n+1} = -\frac{1}{\Delta t}\boldsymbol{C}^t\mathrm{u}^n + \boldsymbol{C}^t\boldsymbol{M}^{-1}\left(\boldsymbol{B}(\boldsymbol{u})\mathrm{u}^n + \boldsymbol{D}_{\boldsymbol{u}}\mathrm{u}^n - \boldsymbol{f}_{\boldsymbol{u}}{}^n\right) , \qquad (4.2.1)$$

$$\boldsymbol{D}_{\phi}\phi^n = -\boldsymbol{C}_{\phi}^t\,\mathrm{u}^n\mathrm{b} + \boldsymbol{f}_{\phi}^n , \qquad (4.2.2)$$

$$\mathrm{u}^{n+1} = \mathrm{u}^n + \Delta t\,\boldsymbol{M}^{-1}\left[\boldsymbol{C}\mathrm{P}^{n+1} - \left(\boldsymbol{B}(\boldsymbol{u})\mathrm{u}^n + \boldsymbol{D}_{\boldsymbol{u}}\mathrm{u}^n\right) + \boldsymbol{f}_{\boldsymbol{u}}{}^n\right] , \qquad (4.2.3)$$

$$\mathrm{T}^{n+1} = \mathrm{T}^n + \Delta t\,\boldsymbol{M}^{-1}\left[-\left(\boldsymbol{B}(\boldsymbol{u})\mathrm{T}^n + \boldsymbol{D}_{\boldsymbol{T}}\mathrm{T}^n\right) + \boldsymbol{f}_{\boldsymbol{T}}{}^n\right] . \qquad (4.2.4)$$

Because the matrix $\boldsymbol{C}^t\boldsymbol{M}^{-1}\boldsymbol{C}$ in Eq. (4.2.1) is Laplacian in discretized form using a mixed finite element basis set and Galerkin's method, the matrix $\boldsymbol{C}^t\boldsymbol{M}^{-1}\boldsymbol{C}$ is a sparse positive definite symmetric matrix. Similarly, the matrix $\boldsymbol{D}_{\phi}$ in Eq. (4.2.2) becomes a sparse symmetric-positive-definite matrix. In analyses of the Czochralski melt flow, the most severe computational load regarding memory and CPU times is the task which solves the Poisson equations of a pressure and an electric potential. Thus, it is necessary to solve Eqs. (4.2.1) and (4.2.2) in away which can efficiently be performed within the constraints of memory size and CPU time.

4.2.2 Conjugate Gradient Method [4.3]

The Poisson equations, Eqs. (4.2.1) and (4.2.2) can be rewritten as

$$[S]\{X\} = \{f\} , \qquad (4.2.5)$$

where [S] is the Laplacian matrix, {X} is the pressure vector or the electric potential vector, and {f} is the right hand side vector.

In the conjugate gradient method, a solution x_{k+1} at step k+1 can be proceeded iteratively with some estimated solutions of x_k, α_k and p_k at previous step k;

$$x_{k+1} = x_k + \alpha_k p_k \ , \tag{4.2.6}$$

where α_k is a scalar value, which is defined later, and p_k is the vector to be searched along a direction such that the norm of the residual vector r_k is minimized.

For a symmetric matrix, the following functional can be defined:

$$F(\mathbf{x}) = (\mathbf{x}, S\,\mathbf{x}) - (\mathbf{x}, 2\mathbf{f}) \ . \tag{4.2.7}$$

Substitution of Eq.(4.1.6) into Eq.(4.2.7) yields to

$$\begin{aligned} F(x_{k+1}) &= (x_k + \alpha_k p_k,\ S(x_k + \alpha_k p_k)) - (x_k + \alpha_k p_k,\ 2f) \\ &= F(x_k) - 2\alpha_k(p_k, r_k) + \alpha_k^2(p_k,\ Sp_k) \ , \end{aligned} \tag{4.2.8}$$

where r_k is the residual vector.

If the coefficient of α_k^2 is positive, Eq.(4.2.8) is quadratic form with respect to α_k. Thus, α_k can determined by

$$\alpha_k = \frac{(r_k, r_k)}{(p_k, Sp_k)} \ . \tag{4.2.9}$$

The residual vector r_{k+1} can be updated as

$$r_{k+1} = r_k - \alpha_k S p_k \ . \tag{4.2.10}$$

A new vector of search direction can be chosen from the new basis, and iteration continues until the residual vector r_{k+1} becomes acceptably small. The new vector of search direction p_{k+1} is selected such that it is the conjugate to all previous vectors of search directions $\beta_k p_k$. At each step, the search direction vector p_k can be updated as

$$p_{k+1} = r_{k+1} + \beta_k p_k \ . \tag{4.2.11}$$

A scalar β_k can be determined to become orthogonal to S.

$$\begin{aligned}(p_{k+1}, Sp_k) &= \left(r_{k+1} + \beta_k p_k,\ Sp_i\right) \\ &= (r_{k+1}, Sp_k) + \beta_k (p_k,\ Sp_k) \\ &= (r_{k+1}, Sp_k) + \beta_k (p_k,\ Sp_k) \\ &= 0 \ .\end{aligned} \tag{4.2.12}$$

Therefore, β_k is given by

$$\beta_k = -\frac{(r_{k+1},\ Sp_k)}{(p_i, Sp_k)} \ , \tag{4.2.13}$$

Using Eqs.(4.2.11) and (4.2.13), the vector p_k can be determined from

$$p_{k+1} = r_{k+1} + \beta_i p_i \ . \tag{4.2.14}$$

Applying the conjugate gradient method to the Poisson equation of a pressure or an electric potential, the matrix and vectors in Eq.(4.3.1) specifically correspond to the following matrices and vectors,

For the Poisson equation of the pressure:

$$[S] = \boldsymbol{C}^t \boldsymbol{M}^{-1} \boldsymbol{C} \ , \tag{4.2.15}$$

$$\{X\} = \{P^n\} \ , \tag{4.2.16}$$

$$\{f\} = -\frac{1}{\Delta t} \boldsymbol{C}^t u^n + \boldsymbol{C}^t \boldsymbol{M}^{-1}\left(\boldsymbol{B}(u) u^n + \boldsymbol{D}_u u^n - f_u^n\right) \ . \tag{4.2.17}$$

For the Poisson equation of an electric potential:

$$[S] = \boldsymbol{D}_{\phi} \ , \tag{4.2.18}$$

$$\{X\} = \left\{\phi^{n}\right\} \ , \tag{4.2.19}$$

$$\{f\} = -\boldsymbol{C}_{\phi}^{t} u^{n} b + f_{\phi}^{n} \ , \tag{4.2.20}$$

In the equations, the superscript n denotes the value at tine step n while the subscript k denotes the iteration step k. And also, the upper case P denotes the the pressure in order to be distinguished from the vector of searching direction p.

As a result, the algorithm to solve the Poisson equation of either a pressure or an electric potential based on the the conjugate gradient method is described as follows:

< STEP 0 >

Initialize x_k by choosing an arbitrary variable x_O. In general, the values at previous time step n are used.

Then, calculate the initial residual vector r_o and the initial vector of searching direction p_o. Initially, p_o set to r_o because the value β_k can be set to zero,

$$x_k = x_o \tag{4.2.21a}$$

$$r_k = \{f\} - Sx_k \tag{4.2.21b}$$

$$p_k = r_k \tag{4.2.21c}$$

Set k to zero

$$k \leftarrow 0 \tag{4.2.21d}$$

< STEP 1>

Calculate Sp_k

< STEP 2 >

Calculate values of scalar α_k and β_k

$$\alpha_k = \frac{(r_k, r_k)}{(p_k, Sp_k)} \tag{4.2.22}$$

$$\beta_k = -\frac{(r_{k+1}, Sp_k)}{(p_i, Sp_k)} \tag{4.2.23}$$

< STEP 3 >

Update the residual vector r_{k+1}, the vector of searching direction p_{k+1}, and the value of x_{k+1}

$$r_{k+1} = r_k - \alpha_k Sp_k$$

$$p_{k+1} = r_{k+1} + \beta_k p_k$$

$$x_{k+1} = x_k + \alpha_k p_k$$

< STEP 4 >

Check whether x_{k+1} reaches to the converged value such that a mean residual norm becomes small. Return to < STEP 1 >, and repeat the procedure from < STEP 1> to < STEP 4 > until the convergence is obtained.

Fig.4.2.1 summarizes the overall flow chart for magneto-thermal-hydraulic flow analysis based on the conjugate gradient method.

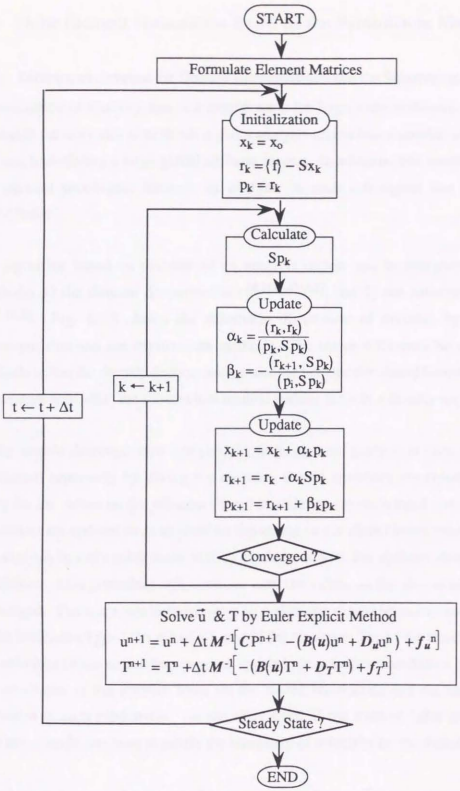

Fig. 4.2.1 Overall flow chart for magneto-thermal-hydraulic flow analysis based on the conjugate gradient method

4.3 Finite Element Formulation Based on the Substructure Method

4.3.1 Differences Between the Domain Decomposition and the Substructure Methods

Minimization of memory size is a crucial issue for large scale problems. One way to minimize memory size is to divide a given analysis region into a number of sub-regions without formulating a large global stiffness matrix. In addition, this method is suitable for parallel processing because an analysis in each sub-region can be executed individually.

An algorithm based on division of an analysis region can be categorized into two methods: 1) the domain decomposition [4.2],[4.4],[4.5], and 2) the substructure method [4.6]-[4.8]. Fig. 4.3.1 shows the schematic illustration of division by the domain decomposition and the substructure methods. The major difference between the two methods is that the domain decomposition method updates the shared boundary values in an iterative way while the substructure method updates them in a directly way.

In the domain decomposition analysis, the finite element analysis in each subdomain is performed separately by giving the tentative shared boundary conditions. After the analysis, the values on the adjacent shared boundaries are exchanged and the boundary conditions are updated so as to correlate the values on the shared boundaries. And again, the analysis in each subdomain will be carried out with the updated shared boundary conditions. This procedure will continue until the values on the shared boundaries are converged. There are two iterative ways to update the shared boundary conditions [4.2] : 1) the Dirichelet Type (the velocity), and 2) the Neumann Type (the traction force). If the velocities on the shared boundary are updated, the constraint conditions have to satisfy the continuity of the traction force on the shared boundaries and the incompressible condition in each subdomain. On the other hand, if the traction force is updated, the constraint conditions have to satisfy the continuity of velocities on the shared boundaries.

The domain decomposition method is advantageous for parallel processing. Because the tentative boundary conditions are given, the finite element analysis in each subdomain can be done separately. However, CPU time becomes enormous due to the iterative method

in updating the values of the shared boundaries, which is a fatal disadvantage for a transient large scale problem. In addition, the incompressible condition is difficult to be satisfied.

On the contrary, since the substructure method is the direct method in solving the vales on the shared boundaries, it does not require as much CPU time as the domain decomposition method does. The substructure method also can satisfy the incompressible condition because it just rearranges the global matrix and memorize a part of the global matrix instead of formulating the entire global matrix. Therefore, compared with the domain decomposition method, the substructure method is more practical for a transient large scale problem in respect of memory size and CPU time than the domain decomposition method.

In the substructure method, each substructure is idealized as an assemblage of finite elements, and all internal degrees of freedom are statically condensed out [4.3]. As a result, the total structure stiffness can be formed by assembling the condensed substructure stiffness matrices. In other words, a substructure is used in the same way as an individual finite element with the internal freedom that are reduced by static condensation prior to the element assemblage process. If an analysis region can be divided into the same geometry, only one condensed substructure stiffness matrix is required, which results in minimization of the memory requirements. However, the disadvantage of the substructure method is that even though it is not necessary to formulate the global stiffness matrix, the memory requirements sill tends to become large. Particularly, when the number of substructures increases, the number of the variables on the shared boundaries also increases and the memory requirement for both internal and shared variables become comparable. Therefore, the further improvement is necessary to minimize the memory size.

4.3.2 Theory of the Substructure Method

Let us consider the following Poisson equation:

$$[S]\{X\} = \{f\} \ , \qquad (4.3.1)$$

where [S] is Laplacian matrix, {X} is the pressure or electric potential vectors, and {f} is the right hand side vector.

Let us invoke the substructure method and divide an analysis region into k substructures. As a result, an analysis region is mainly decomposed into two parts: k numbers of substructures Ω consisting of internal variables and the shared boundary region γ consisting of boundary variables. Fig.4.3.2 shows the configurations of the global stiffness matrices of Laplacian matrix for the conventional method (Fig.4.3.2 a)) and the substructure method (Fig.4.3.2 b)). By employing the substructure method to divide an analysis region into k substructures with m internal variables in each substructure and into a shared boundary with n shared boundary variables, the symmetric definite matrix of the global stiffness matrix can be rearranged as shown in Fig.4.3.2 with S_{ii} [m x m], S_{bi} [n x m] and S_{bi}^T [m x n], and also S_{bb} [n x n].

Consequently, after employing the substructure method, Eq. (4.3.1) can be rewritten as follows:

$$\begin{bmatrix} S_{ii} & S_{bi}^T \\ S_{bi} & S_{bb} \end{bmatrix} \begin{Bmatrix} X_i \\ X_b \end{Bmatrix} = \begin{Bmatrix} f_i \\ f_b \end{Bmatrix}, \qquad i=1,\ldots\ldots k \qquad (4.3.2)$$

where X_i and X_b are the vectors of pressures or electric potentials to be retained (the internal variables) and condensed out (the shared boundary variables), respectively. The matrices S_{ii} is the stiffness matrix corresponding to the internal variables, the matrices S_{bi} and S_{bi}^T are the stiffness matrices corresponding to the internal and the shared boundary variables, and the matrices S_{bb} is the stiffness matrix corresponding to the shared boundary variables.

In the substructure method, the Poisson matrix equation is condensed out by eliminating the internal variables and yields

$$\overline{[S_{bb}]}\{X_b\} = \overline{\{f_b\}}, \qquad (4.3.3)$$

where

$$\overline{[S_{bb}]} = [S_{bb}] - \sum_{i=1}^{k} [S_{bi}][S_{ii}]^{-1}[S_{bi}]^T \ , \tag{4.3.4}$$

$$\overline{\{f_b\}} = \{f_b\} - \sum_{i=1}^{k} [S_{bi}][S_{ii}]^{-1}\{f_i\} \ . \tag{4.3.5}$$

Once the shared boundary variables $\{X_b\}$ is obtained by solving Eq. (4.3.3) – (4.3.5), the internal variables $\{X_i\}$ can be determined as,

$$\{X_i\} = -[S_{ii}]^{-1}[S_{bi}]^T\{f_b\} + [S_{ii}]^{-1}\{f_i\} \ . \tag{4.3.6}$$

Since the matrix $[S_{ii}]$ is the positive-definite-sparse [m x m] matrix as shown in Fig.4.3.2, the skyline method combined with LDU (the Cholesky factorization) decomposition is used to restore the matrix $[S_{ii}]$. Although the matrices $[S_{bi}]$ and $[S_{bi}]^T$ are sparse, the matrices $[S_{bi}][S_{ii}]^{-1}$ and $[S_{ii}]^{-1}[S_{bi}]^T$ become condensed matrices. Thus, it is necessary to restore either the full [n x m] matrices $[S_{bi}][S_{ii}]^{-1}$ or the full [m x n] matrices $[S_{ii}]^{-1}[S_{bi}]^T$. Similarly, the matrix $[S_{bb}]$ is positive-definite-sparse, but the matrix $\overline{[S_{bb}]}$, which is the condensation of $[S_{bb}]$, becomes the dense symmetric matrix. in restoring the matrix $\overline{[S_{bb}]}$, the lower triangular matrix of $\overline{[S_{bb}]}$ is stored.

If a certain number of substructures has the same configuration and boundary condition, it is required to formulate and restore only the matrices $[S_{ii}]$ and either $[S_{bi}][S_{ii}]^{-1}$or $[S_{ii}]^{-1}[S_{bi}]^T$ for one substructure instead of the entire global matrix. Therefore, the minimization of memory storage would result. Since the matrices $[S_{ii}]$, $[S_{bi}][S_{ii}]^{-1}$ and $\overline{[S_{bb}]}$ are independent of time, once these matrices are formed and stored in memory, the calculations can be done by backward and forward substitution without reformulating the substructure matrices at each time step. As a results, the CPU time as well as memory storage will be minimized.

4.3.3 Numerical Algorithm Based on the Substructure Method

The algorithm for magneto-thermal-hydrodynamic flows is summarized as follows:

< STEP 0>

The matrices $[S_{ii}]$, $[S_{bi}][S_{ii}]^{-1}$ and $[\overline{S_{bb}}]$ are formed and are stored in the memory,

< STEP 1 >

The shared boundary variables $\{X_b\}$ with corresponding to P or ϕ is determined by solving Eq. (4.3.3) – (4.3.5),

$$[\overline{S_{bb}}]\{X_b\} = \{\overline{f_b}\} \ , \tag{4.3.3}$$

where

$$[\overline{S_{bb}}] = [S_{bb}] - \sum_{i=1}^{k} [S_{bi}][S_{ii}]^{-1}[S_{bi}]^T \ , \tag{4.3.4}$$

$$\{\overline{f_b}\} = \{f_b\} - \sum_{i=1}^{k} [S_{bi}][S_{ii}]^{-1}\{f_i\} \ . \tag{4.3.5}$$

< STEP 2 >

The internal variables $\{X_i\}$ in each substructure are determined by back substitution of Eq. (4.3.6):

$$\{X_i\} = -[S_{ii}]^{-1}[S_{bi}]^T\{f_b\} + [S_{ii}]^{-1}\{f_i\} \ . \tag{4.3.6}$$

< STEP 3 >

The velocity and the temperature are determined by applying the Euler explicit method of Eqs. (4.2.3) and (4.2.4), respectively:

$$u^{n+1} = u^n + \Delta t\, \boldsymbol{M}^{-1}\left[\boldsymbol{C}P^{n+1} - (\boldsymbol{B}(\boldsymbol{u})u^n + \boldsymbol{D}_u u^n) + \boldsymbol{f}_u{}^n\right] \ , \tag{4.2.3}$$

$$T^{n+1} = T^n + \Delta t\, \boldsymbol{M}^{-1}\left[-(\boldsymbol{B}(\boldsymbol{u})T^n + \boldsymbol{D}_T T^n) + \boldsymbol{f}_T{}^n\right] \ . \tag{4.2.4}$$

< STEP 4 >

The convergence of the steady state or the maximum calculating time is checked. It

the conditions is not satisfied, the time step is advanced to the next time step and calculation goes back to < STEP 1 >.

The procedure from < STEP 1> to <STEP 4 > is performed until the convergence is obtained.

Fig. 4.3.3 summarizes the overall flow chart of the substructure method.

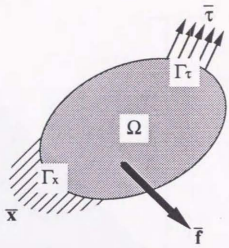

a) Analysis region

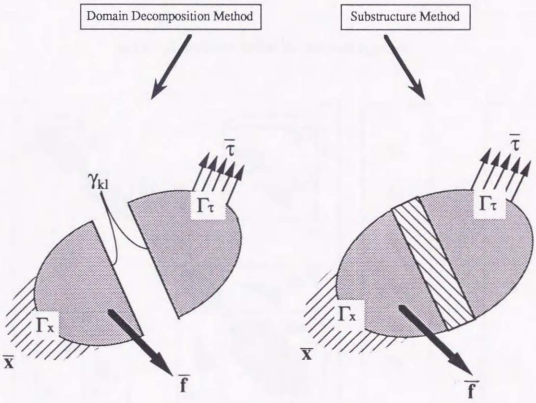

b) Division of an analysis region into two regions by the domain decomposition and the subsutructure methods

Fig. 4.3.1 Comparison of division of ananlysis region by the domain decomposition and the substurcture methods

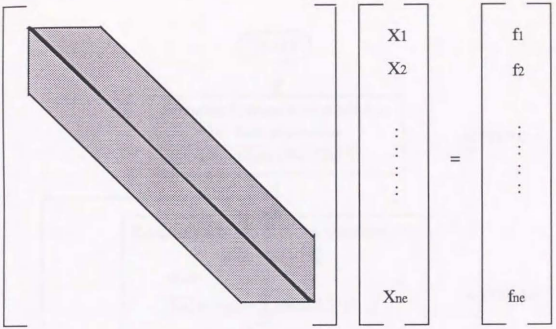

a) Global stiffness matrix for Poisson equation

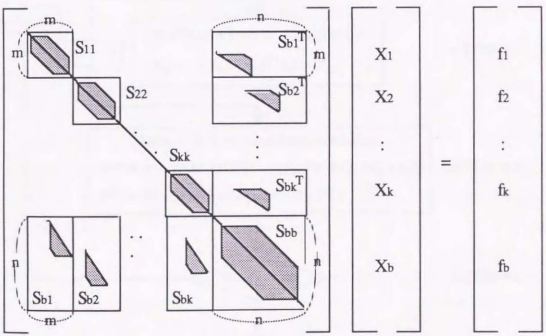

b) Global stiffness matrix employed by substructure method

Fig. 4.3.2 Configuration of global matrices for Laplacian of conventional methods and the substurcture method

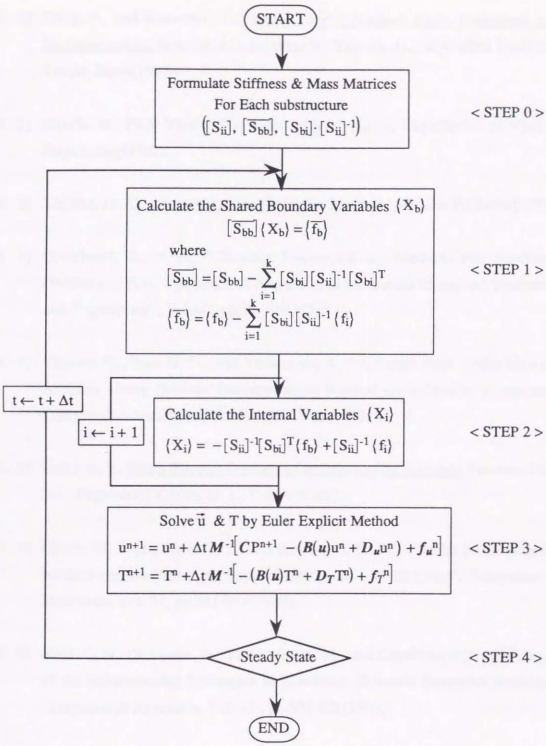

Fig. 4.3.3 Overall flow chart for the substructure method

[References]

[4. 1] Tong, P., and Rossettos, J., Finite Element Method Basic Technique and Implementation, (translated in Japanese by Yagawa, G.), Kyouritsu Publisher, Tokyo, Japan(1983).

[4. 2] Okuda, H., Ph.D Thesis, The University of Tokyo, Department of Nuclear Engineering(1990).

[4. 3] Togawa, H., Conjugate Gradient Method(in Japanese), Kyuiku Publisher(1973).

[4. 4] Glowinski, R., et al., " Domain Decomposition Methods For Nonlinear Problems in Fluid Dynamics", Computational Mechanics In applied Mechanics and Engineering", Vol.40, pp.27-109(1983)

[4. 5] Yagawa, G., Soneda, N., and Yoshimura, S., " A Large Scale Finite Element Analysis Using Domain Decomposition Method on a Parallel Computer", Computers & Structures, Vol.38, pp.615-625(1991).

[4 . 6] Bathe, K. J., Finite Element Procedures in Engineering Analysis, Prentice-Hall, Inc., Englewood Cliffts, N. J., U.S.A.(1982).

[4. 7] Carter, W. T. Jr., Sham, T. L., and Kincho, H. L., " A Parallel Finite Element Method and Its Prototype Implementation on a HyperCube", Computers & Structures, Vol. 31, pp.921-934(1989).

[4. 8] Sheu, C. H., De Roeck, G., Van Laethem, M., and Geyskens, P., " Application of the Substructuring Technique to Non-linear Dynamic Structural Analysis", Computers & Structures, Vol. 35 , pp.593-601(1990).

[4. 9] El-Sayed, M. E. M., and Hsiung, C. K., " Parallel Finite Element Computation with Separate Substructres", Computers & Structures, Vol.36, pp.261-265(1990).

Chapter 5

Analysis Results of Cavity Flows

5.1 Introduction

The analysis results presented in this chapter aim to examine one of main objectives of the thesis. That is to develop and verify the efficient numerical analysis algorithm particularly for melt flow during growth of a large diameter single crystal.

As the scale of the problem increases, more memory size and CPU time are required. For example, a problem with 100,000 degrees of freedom requires more than 1 giga bytes memory and tremendous amount of CPU time [5.1]. Despite recent drastic improvement in the computer technology, it is impossible to carry out an analysis with memory size exceeding 1 giga bytes for long periods of time. A transient incompressible flow in three-dimensions requires calculation of five variables, the velocity ($\vec{u} = (u_x, u_y, u_z)$), the pressure (P) and the temperature (T). Analyses of melt flows in the presence of a magnetic field require the electric potential (ϕ) in addition to the five variables. Consequently, in the case of the melt flow problem, the number of degrees of freedom inherently tends to become large due to the necessity for detailed analysis of transient three-dimensional behavior such as flow patterns and temperature distributions. To perform an analysis of the melt flow within allowable memory size and CPU time, the development of the practical numerical analysis program is imperative.

From the above reasons, the substructure method was applied to the transient finite element analysis program for magneto-thermal-hydraulic flows in three-dimensions. In order to demonstrate the applicability of the substructure methods, two dimensional cavity flows were analyzed.

Analyses of cavity flows in this chapter emphasize on the following three aspects to evaluate the computational performance of the substructure method:

(1) accuracy,

(2) memory requirements, and

(3) CPU time.

The computational performance of the substructure method regarding memory requirements and CPU time was evaluated by varying the number of substructures. The computational performance was also compared with those of single domain analyses by the conjugate gradient method. From the analysis results, the correlations are obtained for memory and CPU requirements with respect to the number of degrees of freedom for melt flow analyses in the Czochralski crystal growth .

5.2 Analysis Model

Two dimensional cavity flows were analyzed to demonstrate the applicability of the proposed substructure method. Since much research on the cavity flow have been conducted, references are available to compare the computational performances with the substructure method [5.2]-[5.4].

The analysis program used the eight-node solid element with a mixed finite element basis function and Galerkin's method such that the bilinear basis functions (Φ_α) is used for the velocity and the piecewise constant value is used for the pressure [5.5]. Because of the interpolation by the piecewise constant value for the pressure, when the substructure method is applied to the Poisson equation of the pressure, the one layer of adjacent substructures needs to be overlapped as illustrated schematically in Fig. 5.2.1.

Fig.5.2.2 describes the analysis model and the boundary conditions used for a two dimensional cavity flow, and also Table 5.2.1 summarizes parameters used for analyses. Because the program was originally developed for three-dimensional analyses, the eight-node solid elements were used. However, since the velocity in the x-direction (u_x) is set to zero value and the upper rid is slid to the y-direction, the analyses should be equivalent to the two dimensional case despite usage of eight-node solid elements.

Analyses for two dimensional cavity flows were carried out by the conjugate gradient method whose algorithm is presented in Chapter 3 and also the substructure method whose algorithm is presented in Chapter 4. An analysis region is divided into total 5041 elements and 10368 nodes. The conjugate gradient method without formulating the global stiffness matrix was applied to analyses of single domain as illustrated in Fig.5.2.3.a).

Figs.5.2.3. b) – e) summarizes the cases of substructure divisions for the substructure method. The substructure method was applied to four types of substructure divisions: 1) 2 x 2 substructures (35 x 35 x 4 internal elements and 141 shared boundary elements), 2) 3 x 3 substructures (23 x 23 x 9 internal elemetns and 280 shared boundary elements), 3) 4x4 substructure (17 x 17 x 16 internal elements and 417 shared boundary elements), and 4) 6x6 substructres (11 x 11 x 36 internal elements and 685 shared boundary elements).

The analyses were performed using the Reynolds number ($Re = \frac{UL}{v} = 100$, where U and L are the characteristic length and velocity, respectively). The computational performances of the substructure method were examined by comparing those of the single domain analyzed by the conjugate gradient method.

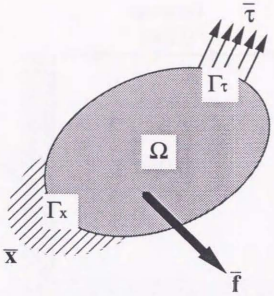

a) Analysis region

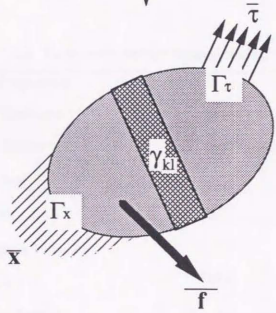

b) Division of an anlysis region into two regions by the substructure method

Fig.5.2.1 Schematic illustration of division of an analysis region into two substrctures

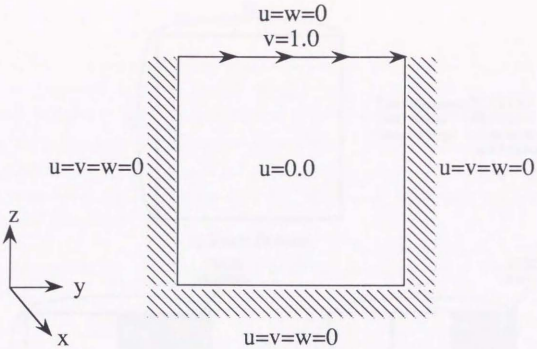

Fig. 5.2.2 Analysis model for two dimensional cavity flows

Table 5.2.1 Parameters for two dimensional cavity flows

[Mesh Division Parameters]	
Total Number of Elements	$71 \times 71 \times 1 = 5041$
Total Number of Nodes	$72 \times 72 \times 2 = 10368$
[Physical Properties]	
Kinematic Viscosity (ν)	0.01
[Analysis Parameters]	
Time Step Size (Δt)	0.001
Criteria for Steady State (ε) $\varepsilon = \dfrac{\sum_{i=1}^{nnode} \lvert v_i^{n+1} - v_i^n \rvert}{\sum_{i=1}^{nnode} \lvert v_i^n \rvert}$	$< 1.0 \times 10^{-6}$

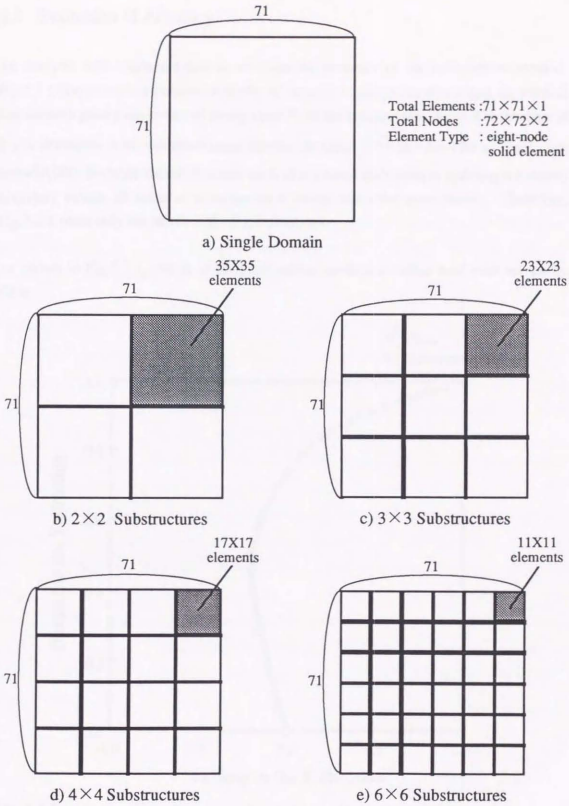

Fig.5.2.3 Cavity flow configuration divided into substructures

5.3 Evaluation of Accuracy

An analysis was conducted first to evaluate the accuracy of the substructure method. Fig.5.3.1 compares computational results of velocity in the y-direction along the vertical line through geometric center of cavity (y=0.5) by the substructure method in the case of 2 x 2 divisions with computational results by Ghia [5.2] for Re=100 at total time step=10,000. Because the substructure method is a direct technique in updating the shared boundary values, all cases of substructure divisions show the same results. Therefore, Fig.5.3.1 plots only the result of the 2 x 2 divisions.

As shown in Fig.5.3.1, results of the substructure method correlate well with results by Ghia.

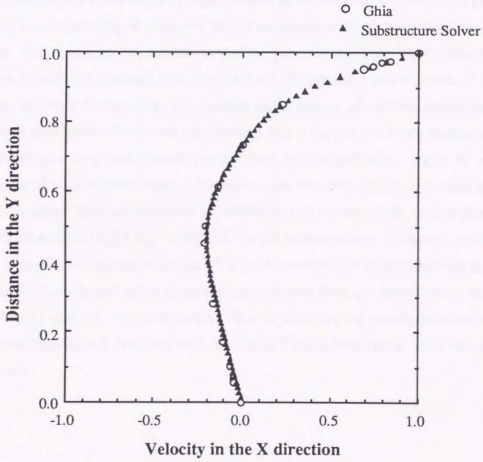

Fig. 5.3.1 Comparison of normalized velocity profile on the vertical center-line for Re=100

(t=0.0~10.0, $\Delta t=1.0 \times 1.0^{-3}$, total time steps=10,000)

5.4 Evaluation of Memory Requirement

Table 5.4.1 summarizes the memory requirements for four cases of mesh divisions by the substructure method and one case of single domain analysis by the conjugate gradient method. Fig.5.4.1 described comparison between the conjugate gradient and the substructure methods for the total memory requirements and the memory requirements for each stored condensed substructure matrices [Sii], $[S_{ii}]^{-1}[S_{bi}]^T$ and $[\overline{S_{bb}}]$.

The solid line in Fig.5.4.1 describes the total memory requirement for the conjugate gradient method. Since the global matrix of the Laplacian is not formulated, the gradient method does not require a large amount of memory.

As shown in Fig.5.4.1, the memory requirements of the substructure method increases up to a 3 x 3 substructuring division and then, it decreases as the number of substructures increases. The reason for the increase is that the geometry of $\boldsymbol{C}^t\boldsymbol{M}^{-1}\boldsymbol{C}$, the discretized Laplacian, in each substructure differs up to 3 x 3. While the gradient matrix $\boldsymbol{C}$ is the same for all the substructures, the lumped mass matrix $\boldsymbol{M}$ differs depending on geometrical conditions. Since each substructure, in the case of 3 x 3 substructre model, has different geometry and boundary conditions, the lumped mass matrix $\boldsymbol{M}$ is not identical for the all substructures. Therefore, the resulting condensed substructure matrices for all of nine substructures are different, and consequently, it is required to restore matrices [Sii], $[S_{ii}]^{-1}[S_{bi}]^T$ and $[\overline{S_{bb}}]$. for all substructures. However, when the analysis region is divided into more than 3 x 3 substructures, it is not necessary to store more than 3 x 3 condensed substructure matrices because there are substructures with the same geometry and boundary conditions. This implies that the substructure method is more appropriate for sub-divisions with more than 3 x 3 substructures, as in the case of cavity flows.

Table 5.4.1 Comparison of memory requirements for cavity flows
(Re=100, Total elements = 71 x 71 x 1, Total nodes = 72 x 72 x 2 = 10,368)

Number of Substructures	Substructure Method				CG Method
	2×2	3×3	4×4	6×6	1
Number of Elements per Substructure	1225	529	289	121	5041
Number of Elements on the Shared Boundary	141	280	417	685	0
Memory Requirement for $[S_{ii}]$ Matrix (MB)	1.410 (0.352×4)	0.913 (0.101×9)	0.369 (0.041×9)	0.104 (0.011×9)	–
Memory Requirement for $[\overline{S_{bb}}]$ Matrix (MB)	0.080	0.315	0.697	1.880	–
Memory Requirement for $[S_{bi}]\cdot[S_{ii}]^{-1}$Matrix (MB)	1.607 (0.402×4)	10.665 (1.185×9)	8.677 (0.964×9)	5.968 (0.663×9)	–
Total Memory Requirement (MB)	10.631	15.109	12.503	10.539	5.240

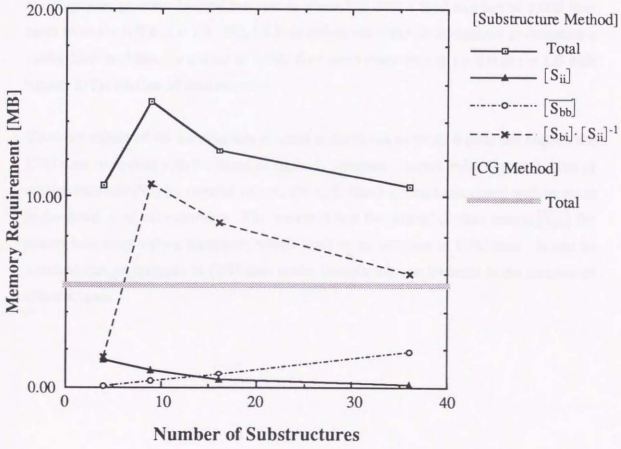

Fig. 5.4.1 Comparison of memory requirements with respect to the number of substructures

5.5 Evaluation of CPU Time

Table 5.5.1 summarizes the total CPU time and the CPU time required for the solver in four cases of mesh division by the substructure method and one case of single domain analysis by the conjugate gradient method. The analyses were performed on Cray Y-MP/8I with the conditions of Re = 100.

The criteria for convergence of the conjugate gradient method was set to 1.0×10^{-10}, and the size of time step was set to 1.0×10^{-3}. The number of iterations required more than 300 steps at the initial time step, and consequently the averaged number of iterations of the conjugate gradient method resulted in about 150 over a total number of 1,000 time steps from t = 0.0 to t = 1.0. Fig.5.5.1 describes the CPU time required to calculate a cavity flow problem for a total of 1,000 time steps from time at t = 0.0 to t = 1.0 with respect to the number of substructures.

Since the solver of the substructure method is the direct method, it does not require the CPU time compared with the iterative method. However, despite reduction in the size of skyline matrices [Sii] for internal values, the CPU time increases associated with increase in the number of substructures. The reason is that the size of skyline matrix $[\overline{S_{bb}}]$ for shared boundary values increases, which leads to an increase in CPU time. It can be assumed that an increase in CPU time scales linearly with an increase in the number of substructures.

Table 5.5.1 Comparison of CPU time required for cavity flows
(Re=100, Total elements = 71 x 71 x 1, Total nodes = 72 x 72 x 2 = 10,368)

Number of Substructures	Substructure Method				CG Method
	2×2	3×3	4×4	6×6	1
Number of Elements per Substructure	1225	529	289	121	5041
Number of Elements on the Shared Boundary	141	280	417	685	0
CPU Time Required for Matrix Formulation (sec)	9.7	16.6	22.2	57.5	-
CPU Time Required for Solver [t=0.0～1.0] (sec)	82.0	93.5	108.5	120.1	473.0
Total CPU Time [t=0.0～1.0] (sec)	396.0	415.7	423.0	527.3	751.4

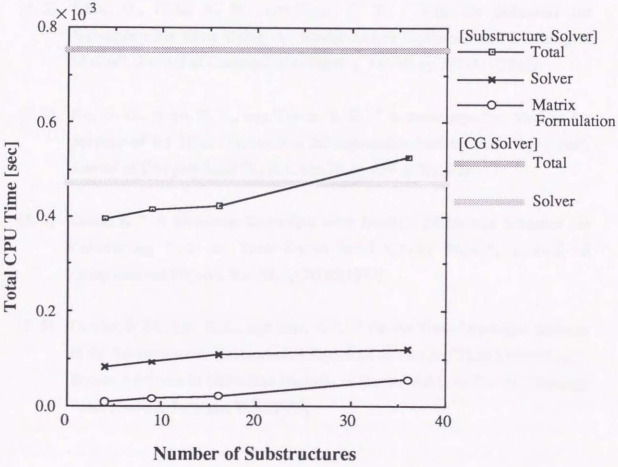

Fig. 5.5.1 Comparison of CPU time with respect to the number of substructures

[References]

[5. 1] Yoshioka, A., Yagawa, G., Yoshimura,S., and Soneda, N., " A Large Scale Finite Element Analysis by Supercomputer Network"(in Japanese), Proceedings of the 3rd JASME computational mechanics conferences, Tokyo, Japan, pp.195-196(1990).

[5. 2] Ghia, U., Ghia, K. N., and Shin, C. T., " High-Re Solutions for Incompressible Flow Using the Navier-Stokes Equations and a Multigrid Method", Journal of Computational Physics, Vol.48, pp.387-411(1982).

[5. 3] Ku, H. C., Hirsh, R. S., and Taylor, T. D., " A Pseudospectral Method for Solution of the Three-Dimensional Incompressible Navier-Stokes Equations", Journal of Computational Physics, Vol.70, pp.439-462(1987).

[5. 4] Goda, K.," A Multistep Technique with Implicit Difference Schemes for Calculating Two- or Three-Dimensional Cavity Flows", Journal of Computational Physics, Vol.30, pp.76-95(1979).

[5. 5] Gresho, P. M., Lee, R. L., and Sani, R. L., " On the Time-Dependent Solution of the Incompressible Navier-Stokes Equations in Two and Three Dimensions" , Recent Advances in Numerical Methods in Fluids, Vol.1, pp.27- 79, Pineridge Press Limited, Swansea, U.K.(1980).

Chapter 6

Analysis Results of Melt Flows

6.1 Introduction

The objectives of this chapter is to understand the behavior in the melt, particularly, the flow patterns and temperature distributions by the numerical analysis. The analyses were performed for the melt flows in the Czochralski growth of a small and a large diameter single crystals.

First of all, the analysis model and boundary conditions for the melt flow are described. Generally speaking, the boundary conditions, particularly, temperature boundary conditions for melt flows in the Czochralski system are difficult to be exactly defined, because the highly coupled physical phenomena in the high temperature field prevent measurements from being precise. Thus, after the analysis models were described, the boundary conditions for analyses were clarified.

Secondly, analyses of melt flows for a small diameter single crystals were carried out by the conjugate gradient method. The melt flows for a small diameter single crystal were simulated to examine its behavior by applying the various types of boundary conditions such as rotation rates of crystal and crucible, and magnitudes of an external magnetic field. The effect of an external magnetic field was found to suppress both the velocity and the temperature fields significantly at the magnetic field flux density B = 1,000 G. The non-axisymmetric flow pattern was observed when the magnetic field was imposed in the horizontal direction. However, the temperature distribution was not affected by the direction of the external magnetic field since natural convection was much more dominant than the changes in the velocity field due to the application of an external magnetic field.

Since the analyses for melt flows of a large diameter single crystal demand a large amount of memory size and CPU time, the substructure method was introduced. Before the melt

flow analyses for a large diameter single crystal were performed, the bench-mark tests were conducted to investigate the memory size and CPU time required for the conjugate gradient and the substructure methods. There are some periodic characteristics in the condensed out substructure matrices due to the axisymmetric geometry of the Czochralski system. Taking advantage of this periodic characteristics, the required memory usage for analyses of large size melt flows was improved and the resulting computational performance for both methods were compared. It was found that the memory usage for the substructure method was reduced to 1/1,000 of memory usage for the skyline method and the CPU time was minimized to 1/5 of CPU time for the conjugate gradient method. Furthermore, the correlations of memory requirement and CPU time with the number of degrees of freedom were derived based on the results of cavity flows in order to assess the memory size and CPU time for a large scale problem.

Finally, analyses of melt flows for a large diameter single crystals were performed by dividing the melt flow region into eight-substructures. The analysis results showed dominant effects of natural convection on the melt flows.

6.2 Analysis Model

Fig.6.2.1 schematically illustrates the analysis model of melt flows in the Czochralski crucible with radius R_c during the growth of a single crystal with radius R_s.

The shapes of both free surface and crystal/melt interface are assumed to be flat and stationary. Thus, the analysis will neglect convexity or concavity of the interface as well as ripples and menisci of the free surface, which change associated with the gradual depletion of the melt level by pulling up the crystal. Although the shapes are not exactly flat and stationary in a real situation, this bulk flow approximation can be valid in the time scale that the analysis is applied [6.1]-[6.3].

The finite element mesh division for the melt flows is also illustrated in Fig.6.2.1. The mesh division was performed so as to have size of elements as uniform as possible throughout an analysis region as shown in Fig.6.2.1. If there is a large difference in the

size between elements, it would cause unnecessary numerical oscillation or numerical errors.

For the substructure analysis, the analysis region is divided into an assembly of substructures and shared boundary parts with an identical mesh division by taking into account the axisymmetric geometry of the Czochralski crucible and only matrices for one substructure and shared boundary parts are formulated and stored.

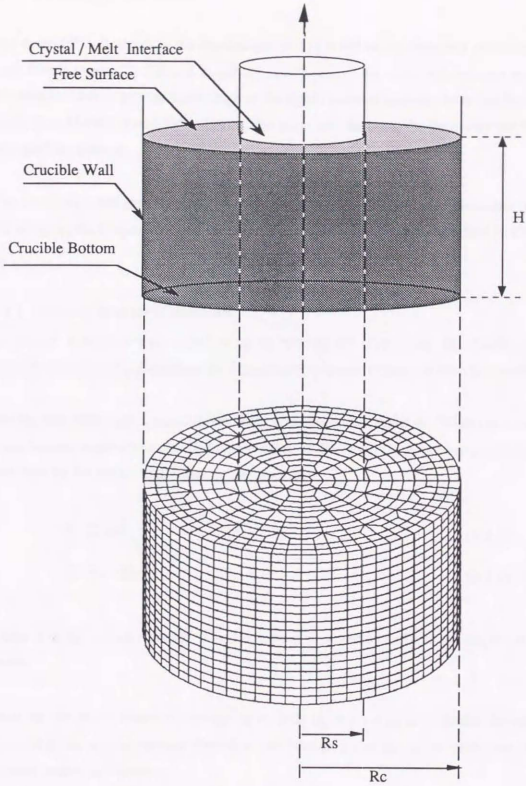

Fig. 6.2.1 Analysis model and finite element mesh for melt flows in the Czochoralski crystal growth

6.3 Boundary Conditions

The most difficult aspect in the detailed analysis is to define the boundary conditions for melt flows, especially thermal boundary conditions. This issue still remains an open problem for lack of precise knowledge of the highly coupled complex heat transfer in the entire Czochlarski system [6.4]. Taking this point into account, the boundary conditions are carefully defined.

The boundary conditions for melt flows are given by either Dirichelet or Neumann type of the velocity, the temperature and the electric potential in the melt as described in Chapter 3.3.

6.3.1 Velocity Boundary Conditions

In general, a single crystal is pulled up by rotating the crystal and the crucible in the opposite directions for dispersing the temperature striations created by natural convection.

For the rigid boundaries, non-slip boundary conditions are employed. When the crystal is rotated at the angular velocity Ω_s in the clockwise direction, the boundary conditions for velocities on the crystal/melt interface are given by

$$\vec{u} \cdot \vec{n} = 0 , \tag{6.3.1}$$

$$\vec{u} \cdot \vec{t} = r\,\Omega_s , \tag{6.3.2}$$

where $\vec{u}$ is the velocity vector, $\vec{n}$ is the normal unit vector and $\vec{t}$ is the tangential unit vector.

Since the crucible is rotated at the angular velocity Ω_c in the counterclockwise direction as opposed to the crystal rotation direction, the boundary conditions for velocities on the crucible bottom are given by

$$\vec{u} \cdot \vec{n} = 0 , \tag{6.3.3}$$

$$\vec{u} \cdot \vec{t} = r\,\Omega_c \ , \tag{6.3.4}$$

Similarly, the velocity boundary conditions on the crucible wall are given by

$$\vec{u} \cdot \vec{n} = 0 \ , \tag{6.3.5}$$

$$\vec{u} \cdot \vec{t} = R_c\,\Omega_c \tag{6.3.6}$$

where R_c is the radius of the Czochralski crucible.

In defining the boundary conditions on the free surface, the consideration of Marangoni convection rises as a problem. Since there is no reliable data for the coefficient of surface tension, it is difficult to determine the effects of Marangoni convection. However, it is found that the effects of Marangoni convection on the melt can be negligible because the analysis results without considering Marangoni convection showed good correlation with the experimental results in the temperature distribution [6.4],[6.5]. Thus, the effects of Marangoni convection is not considered here, and free slip boundary conditions are applied to the free surface as follows:

$$\left(\vec{n} \cdot \vec{\nabla}\right)\left(\vec{u} \cdot \vec{t}\right) = 0 \ . \tag{6.3.7}$$

6.3.2 Thermal Boundary Condition

As mentioned before, the temperature boundary condition is quite difficult to be specified. The most appropriate method would be to combine with the global model so as to use the resulting temperature distribution from the global model as the boundary conditions for detailed analyses. But, this approach is not presently feasible because it requires a large amount of memory size and CPU time. Another way is to combine with the experimental data. However, experiments are difficult to conduct and measure precisely, and also the data for a large diameter single crystal are not available. Therefore, the temperature boundary conditions are determined empirically based on experiments and references [6.1] – [6.4].

For the temperature boundary conditions on the crystal/melt interface, the temperature can be assumed to take the constant value at the melting point. Therefore, the temperature boundary condition is given by

$$T = T_s \ , \tag{6.3.8}$$

where T_s is the melting point.

The temperature profiles on the crucible bottom are assumed to be a linear function of the crucible radius (r). Thus, the temperature boundary condition on the crucible bottom is given as follows:

$$T = T_c(r) = T_{cm} + \left(T_{wb} - T_{cm} \right) \frac{r}{R_c} \ , \tag{6.3.9}$$

where T_{cm} and T_{wb} are temperature at the middle of the crucible bottom and at the bottom edge of the crucible.

Similarly, the temperature boundary condition on the crucible wall are assumed to be a linear function of the crucible height from the bottom (z) and are given as follows:

$$T = T_w(z) = T_{wb} + \left(T_{wt} - T_{wb} \right) \frac{z}{H} \ , \tag{6.3.10}$$

where T_{wt} is the temperature at the upper edge of the crucible and H is the height of the crucible.

Although the heat exchange due to radiation and convection exists on the free surface, the free surface is assumed to be adiabatic, namely no heat transfer occurs between the melt and outer boundary. Thus, the thermal boundary condition on the free surface is given by

$$\vec{n} \cdot \vec{\nabla} T = 0 \ . \tag{6.3.11}$$

6.3.3 Magnetic Field Boundary Conditions

The crucible can be assumed to be made of non-conducting walls. Since the current on the crucible and on the free surface can be assumed to be zero, boundary conditions for the electric potential can be defined as

$$\vec{n} \cdot \vec{\nabla} \phi = 0 \ . \tag{6.3.12}$$

However, the center of the crucible bottom is set as follows:

$$\phi = 0 \ . \tag{6.3.13}$$

Thus, all boundary conditions for the melt flow are summarized in Fig.6.3.1.

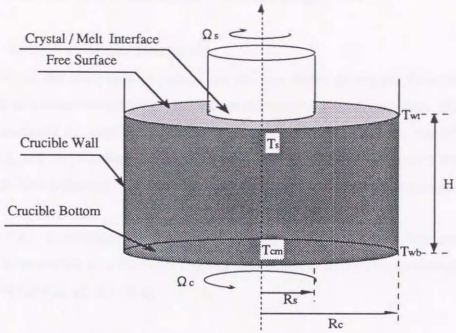

[Boundary Conditions]

(A) Crucible Bottom ($0 \leqq r \leqq R_c,\ z = 0$)

$\vec{u} \cdot \vec{n} = 0$ $\qquad T = T_c(r) = T_{cm} + \left(T_{wb} - T_{cm} \right) \frac{r}{R_c}$

$\vec{u} \cdot \hat{t} = r\,\Omega_c$

(B) Crucible Wall ($r = R_c,\ 0 \leqq z \leqq H$)

$\vec{u} \cdot \vec{n} = 0$ $\qquad T = T_w(z) = T_{wb} + \left(T_{wt} - T_{wb} \right) \frac{z}{H}$

$\vec{u} \cdot \hat{t} = R_c\,\Omega_c$

(C) Free Surface ($R_s \leqq r \leqq R_c,\ z = H$)

$\left(\vec{n} \cdot \vec{\nabla}\right)\left(\vec{u} \cdot \hat{t}\right) = 0$ $\qquad \vec{n} \cdot \vec{\nabla} T = 0$

(D) Crystal/Melt Interface ($0 \leqq r \leqq R_c,\ z = H$)

$\vec{u} \cdot \vec{n} = 0$ $\qquad T = T_s$

$\vec{u} \cdot \hat{t} = r\,\Omega_s$

Magnetic Field: $B(r, t) = \text{constant}$

Electric Field: Insulation

Fig. 6.3.1 Boundary conditions for melt flows of the Czochoralski crystal growth

6.4 Melt Flows For the Small Diameter Single Crystal

6.4.1 Analysis Parameter Description

First of all, the analysis was carried out for melt flows during the Czochralski crystal growth of a small size single crystal whose diameter was about one inch. The melt flows were analyzed by varying the operating parameters such as rotation rate of crystal and crucible, and magnitudes of an imposed magnetic field in order to examine their effects on the melt flow behavior. The analyses were conducted by the conjugate gradient method.

Table 6.4.1 summarizes the physical properties used for the melt flow analyses. The physical properties are essentially those of silicon that have been experimentally measured in the references [6.2] – [6.4].

Table 6.4.2 summarizes the geometry and operating conditions. The geometry was referred to the small diameter single crystal used in the references [6.3] and [6.6]. For the thermal boundary conditions on the crucible, the temperature profiles on the crucible bottom were given by a linear function of radial distance from the axis and the temperature profiles on the crucible wall were given at the constant value.

Fig.6.4.1 shows the finite element mesh used for the melt flow analyses. The eight-node solid elements were used for the finite element mesh. The velocity was interpolated by the bilinear finite element basis function while the pressure was approximated by the piecewise constant value. As a result, the total number of elements was 7272, and the total number of nodes was 8303, which leads to the total number of degrees of freedom as 40,488. The analysis region was divided into 18 elemetns with $\delta z = 0.15$ cm length in the z-direction and also was divided into 14 elements with $\delta r = 0.225$ cm length in the r-direction as illustrated in Fig.6.4.1.

Table 6.4.3 summarizes totally 6 cases of operating conditions used for the simulations in which the rotation rate of crystal and crucible, and magnitudes of an imposing magnetic field were varied.

For the initial conditions, the melt was assumed to be at the quiescent state. Thus, all initial conditions for the velocity, the pressure, and the electric potential are set to be zero. The initial conditions for the temperature are set to be at 1690 K. Then, the melt flow was analyzed with the time increment size as $\Delta t = 1.0 \times 10^{-3}$.

Table 6.4.1 Physical properties used for melt flow simulations of small diameter silicon single crystal

Physical Properties			
Melt Density	(g / cm^3)	ρ	2.33
Kinematic Viscosity	(cm^2 / s)	υ	0.0043
Volumetric Expansion Coefficient	$(/ K)$	β	1.41×10^{-5}
Thermal Diffusivity	(cm^2 / s)	α	0.125
Electrical Conductivity	$(/ \Omega\, cm^2)$	σ	1.25×10^4

Table 6.4.2 Geometry and thermal operating parameters for melt flow simulations of small diameter silicon crystal

Parameters			
Crucible Radius	(cm)	R_c	3.150
Crystal Radius	(cm)	R_s	1.125
Melt Depth	(cm)	H	3.600
Crystal / Melt Interface Temperature	(K)	T_s	1685.0
Crucible Center Temperature	(K)	T_{cm}	1705.0
Crucible Wall Temperature at the bottom	(K)	T_{wb}	1745.0
Crucible Wall Temperature at the top	(K)	T_{wt}	1745.0

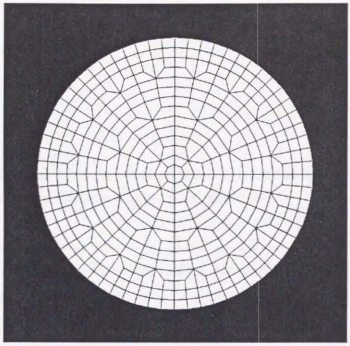

a) Horizontal view of the finite element mesh in the melt region

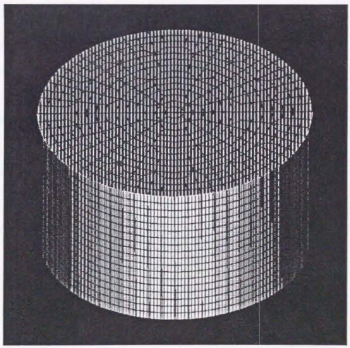

b) Detailed view of the finite element mesh in the melt region

Fig.6.4.1 Finite element mesh in the melt region
(total number of elements = 7,272, total number of nodes = 8,303)

Table 6.4.3 Operating parameters of velocity and magnetic fields for simulations of small diameter single crystal melt flows

Case	Crystal rotaion rate (rpm)	Crucible rotaion rate (rpm)	Magnetic Field in the x-direction (G)	Magnetic Field in the z-direction (G)
1	30.0	0.0	0.0	0.0
2	30.0	−15.0	0.0	0.0
3	30.0	−15.0	0.0	1,000.0
4	30.0	−15.0	1,000.0	0.0
5	30.0	−15.0	0.0	10,000.0
6	30.0	−15.0	10,000.0	0.0

6.4.2 Analysis Results

6.4.2.1 Flow Patterns

Figs.6.4.2 a) – e) show the evolution of the flow patterns on the vertical plane from the elapsed time t = 1.0 sec to t = 30.0 sec for case 2 in which the crystal was rotated at rotation speed of 30 rpm in clockwise and the crucible was rotated at −15 rpm, that is 15 rpm counterclockwise.

At the elapsed time t = 1.0 sec (Fig.6.4.2 a)), the melt flow was still at the quiescent state. But at the elapsed time at t = 7.5 sec (Figs.6.4.2 b)), a large vortex was observed in the middle of the melt near the crucible wall and grew as the elapsed time proceeded. As the elapsed time proceeded furthermore, the second vortex appeared at the top corner of the crucible at the elapsed time t = 22.5 (Figs.6.4.2 c)) and started to grow with pushing the first vortex toward the direction of the center bottom. The first large vortex was assumed to be created by natural convection while the second small vortex assumed to be created by forced convection.

The effects of an external magnetic field on the melt flow patterns can be observed in Figs.6.4.3 a) – c), which show the velocity profile on the vertical plane at the elapsed time t = 30.0 sec. The vector scale of Figs.6.4.3 b) and 6.4.3 c) are ten times as large as that of Fig.6.4.3 a) in order to look into details of the melt flow behavior. Compared with the velocity profile in case 2 (Fig.6.4.3.a)), the magnitude of the velocity in both cases 3 and 4 (Figs.6.4.2 a) and b)) were suppressed due to the Lorentz force ($\vec{J} \times \vec{B}$). In case 3, the magnetic field was imposed in the z-direction. Therefore, the axisymmetric flow pattern was maintained and showed the similar behavior as seen in case 2. On the other hand, since in case 4, the magnetic field was imposed in the x-direction, the way that the vortex was created in case 4 is different form that in cases 2 and 3. As shown in Fig.6.4.3. c), there are two vortices at the upper and the bottom parts of the crucible.

In order to observe the flow field in more details, the velocity profiles at several points are plotted. First of all, the circumferential and vertical velocities along the vertical line are plotted. Figs.6.4.4 a) and 6.4.5 a) describe the circumferential and the vertical velocities in the melt under the crystal outer edge along the vertical line, r = 1.125 cm and θ = 0.0

degree at the elapsed time t = 30.0 sec. Similarly, Figs. 6.4.5 a) and b) describe the circumferential and the vertical velocities in the melt under the free surface close to the crystal along the vertical line, r = 1.125 cm and θ = 0.0 degree at the elapsed time t=30.0 sec. The positive sign for the circumferential velocity designates the clockwise direction and the negative sign designates the counterclockwise direction.

When the crucible was at the quiescent state (case 1), the tendency of the flow behavior showed the similar behavior of case 2 in which the crucible was rotated in the counterclockwise direction. However, when the magnetic field was imposed, the velocity field was drastically suppressed even at the magnetic field flux density B = 1000.0 G. Since the Lorentz force suppresses the normal component of the velocity to the magnetic field, the circumferential velocity would be suppressed when the magnetic field is imposed vertically (B_z). On the contrary, the vertical velocity would be suppressed when the horizontal field is imposed horizontally (B_x). Particularly, the vertical velocity component of case 3 (—+—) showed the larger magnitude than that of case 4 (--+--) as described in Figs. 6.4.5 a) and b).

Secondly, the circumferential and vertical velocities along the horizontal line are plotted. Figs 6.4.6 a) and 6.4.7 a) describe the circumferential velocities along the horizontal line from the axis to the edge of the crucible, z = 3.4 cm and θ = 0.0 degree at the elapsed time t = 30.0 sec. Figs 6.4.6 b) and 6.4.7 b) describe the circumferential velocities along the horizontal line from the axis to the edge of the crucible, z = 1.8 cm and θ = 0.0 degree at the elapsed time t = 30.0 sec. The shaded region in Figs.6.4.6 and 6.4.7 represents the radius of the crystal.

The effects of the rotation of the crucible on the flow fields were not significant near the free surface as shown in Figs.6.4.6 a) and 6.4.7 b). However, in the middle of the melt depth, the difference between the flows in cases 1 and 2 can be observed especially near the crucible wall for the circumferential component and near the axis for the vertical component. Figs.6.4.6 and 6.4.7 also shows the effects due to the presence of a magnetic field on the flow behavior .

When the horizontal magnetic field was imposed, the axisymmetric characteristics of the

flow pattern could be no longer maintained. In fact, Figs.6.4.8 a) – c) describe the non-axisymmetric flow patterns on the horizontal plane near the free surface at z = 3.4 cm, in the middle of the melt depth at z = 1.8 cm, and near the crucible bottom at z = 0.2 cm, respectively. Since the magnetic field was imposed in the x-direction, the velocity in the y-direction was also suppressed as shown in Figs.6.4.8 as well as that in z-direction.

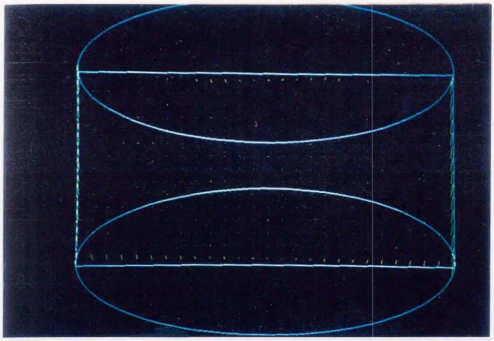

Fig.6.4.2 a)
t = 1.0 sec

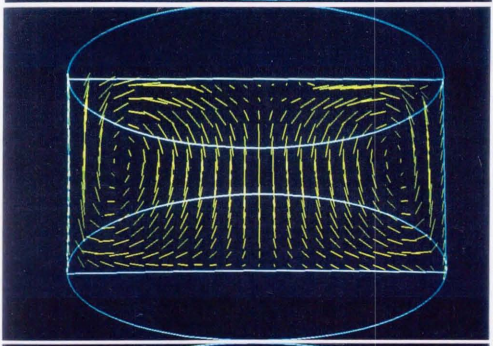

Fig.6.4.2 b)
t = 7.5 sec

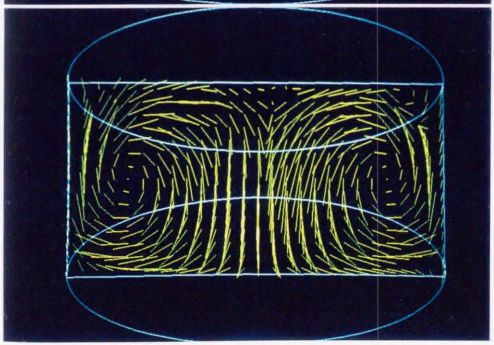

Fig.6.4.2 c)
t = 15.0 sec

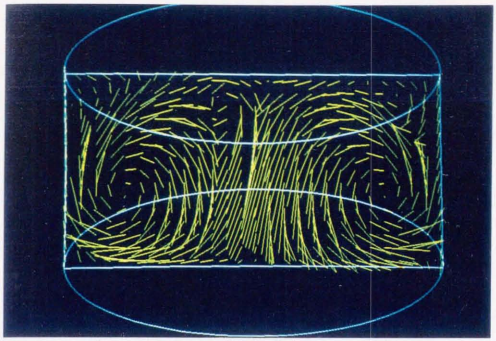

Fig.6.4.2 d)
t = 22.5 sec

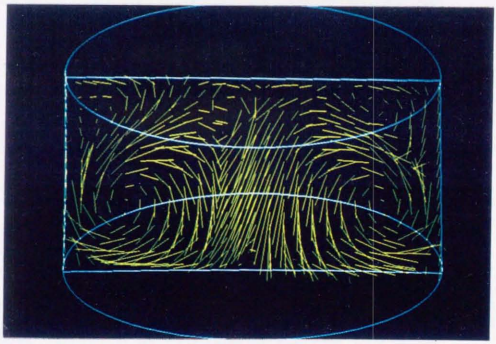

Fig.6.4.2 e)
t = 30.0 sec

Fig.6.4.2 Evolution of velocity profile on the verical plane for case 2

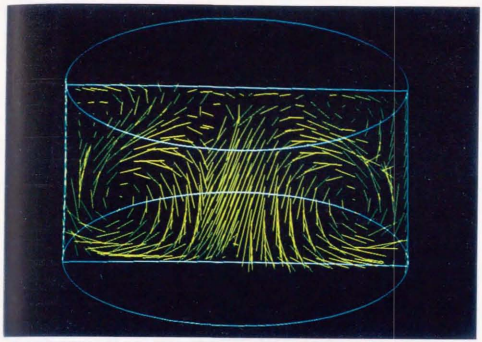

Fig.6.4.3 a)
Case 2
$B_x = 0$ G
$B_z = 0$ G

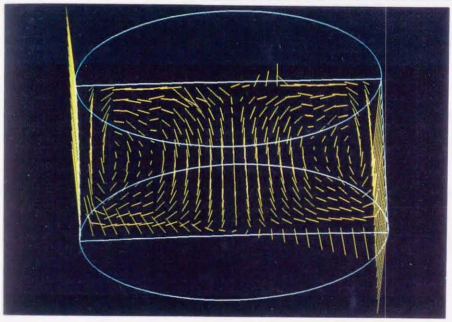

Fig.6.4.3 b)
Case 3
$B_x = 0$ G
$B_z = 1{,}000$ G

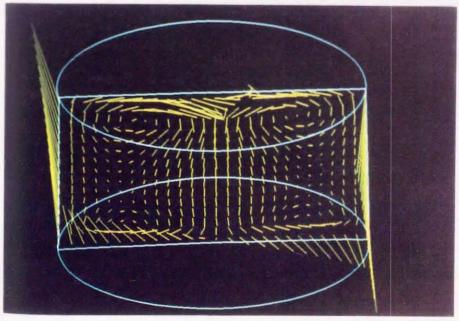

Fig.6.4.3 c)
Case 4
$B_x = 1{,}000$ G
$B_z = 0$ G

Fig.6.4.3 Velocity profile on the vertical plane at the elapsed time t = 30.0 sec

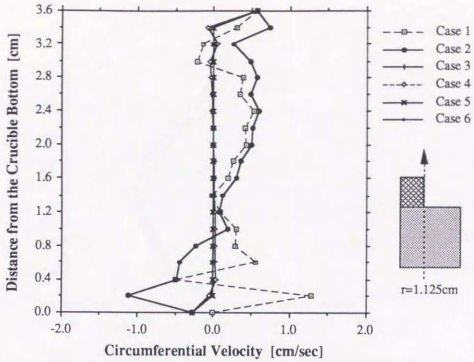

Fig.6.4.4 a) Circumferential velocity profile on the vertical line at r = 1.125 cm and θ = 0.0 degree with respect to distance from the crucible bottom

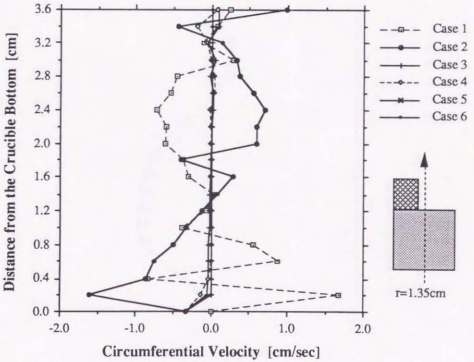

Fig.6.4.4 b) Circumferential velocity profile on the vertical line at r = 1.35 cm and θ = 0.0 degree with respect to distance from the crucible bottom

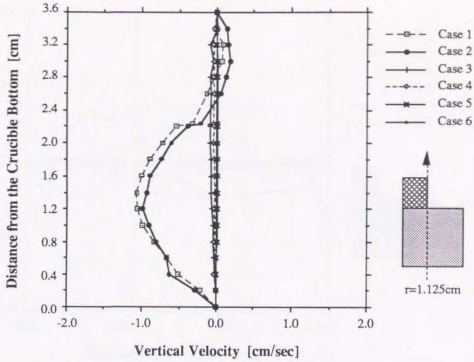

Fig.6.4.5 a) Vertical velocity profile on the vertical line at r = 1.125 cm and θ = 0.0 degree with respect to distance from the crucible bottom

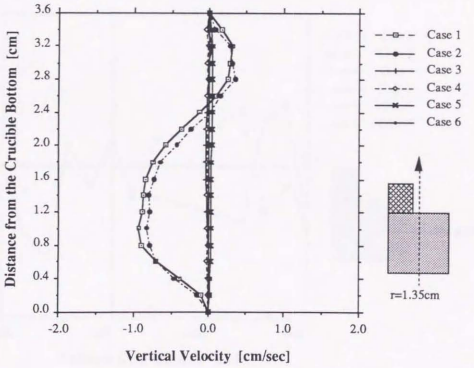

Fig.6.4.5 b) Vertical velocity profile on the vertical line at r = 1.35 cm and θ = 0.0 degree with respect to distance from the crucible bottom

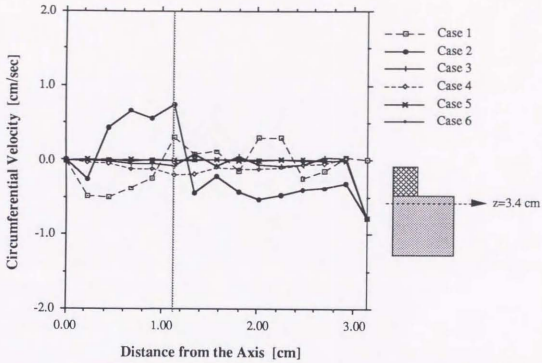

Fig.6.4.6 a) Circumferential velocity profile on the horizontal line at z = 3.4 cm and θ = 0.0 degree with respect to distance from the axis

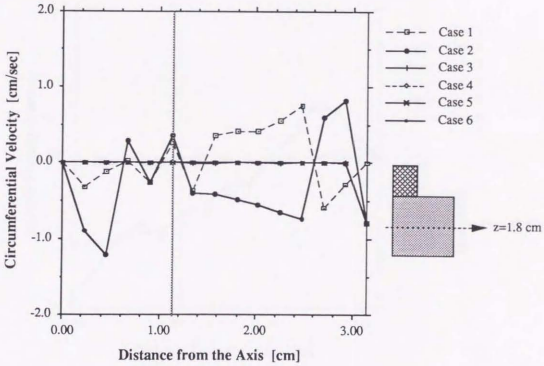

Fig.6.4.6 b) Circumferential velocity profile on the horizontal line at z=1.8 cm and θ = 0.0 degree with respect to distance from the axis

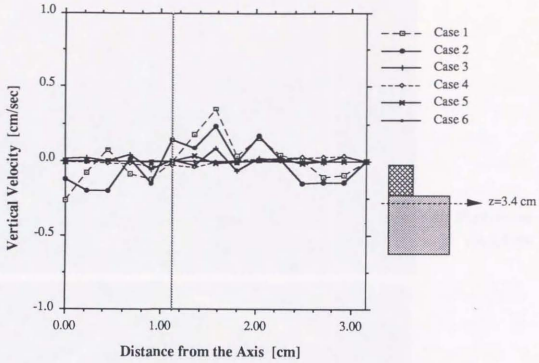

Fig.6.4.7 a) Vertical velocity profile on the horizontal line at r = 3.4 cm and θ = 0.0 degree with respect to distance from the axis

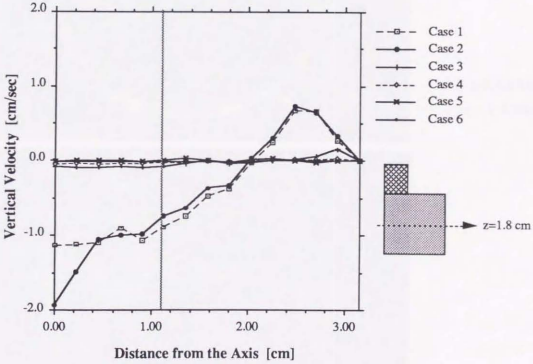

Fig.6.4.7 b) Vertical velocity profile on the horizontal line at r = 1.8 cm and θ = 0.0 degree with respect to distance from the axis

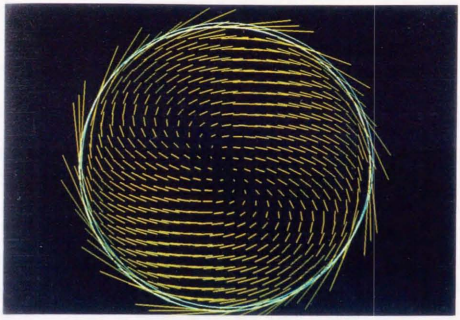

Fig.6.4.8 a)
z = 3.4 cm

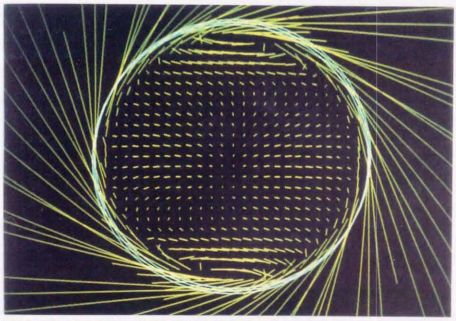

Fig.6.4.8 b)
z = 1.8 cm

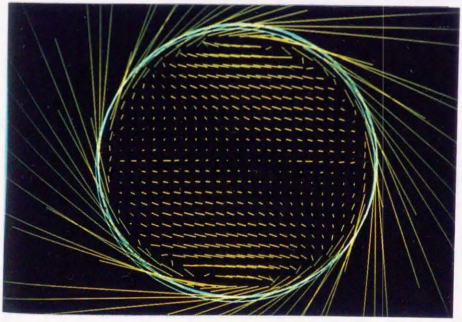

Fig.6.4.8 c)
z = 0.2 cm

Fig.6.4.8 Velocity profile of the case 4 on the horizontal plane at the elapsed time t = 30.0 sec

6.4.2.2 Temperature Distributions

The evolution of the temperature profiles on the vertical plane is shown in Fig.6.4.9 a) – e). Each picture describes the temperature distribution from the elapse time t = 0.0 sec to t = 30.0 sec for case 2 in which both the crystal and the crucible were rotated in the opposite direction with speed of 30 rpm and −15 rpm, respectively. Temperature of the melt varies from a minimum melt temperature T = 1685 K to a maximum melt temperature T = 1745 K. The colors of the isotherm in Figs.6.4.9 varies from blue color to pink color with twenty variation of colors, implying that the corresponding temperature varies from 1685 K to 1745 K with 3 K of the temperature increment in each color.

The evolution of the temperature profiles changes accordingly to that of the velocity profile as depicted in Figs. 6.4.2. At the elapsed time t = 1.0 sec, the flow was still at the quiescent state and the melt remained at the cold temperature. However, the melt was gradually heated up from the hot crucible wall and bottom by natural convection associated with the time evolution. Then, the vortex due to forced convection started to grow such that the convective flows with the high temperature descends from the top edge of the crucible toward the the bottom center direction.

The effects of the magnetic field on the temperature field are described in Figs.6.4.10 a) – c). The flow field is suppressed by the Lorentz force in the presence of a magnetic field. The natural convective flows, which were distributed from the bottom and upper parts of the crucible were significantly reduced. Thus, the temperature evolution shows the temperature layers on the vertical place as shown in Figs.6.4.10 b) and c). The magnitude of the velocity in cases 3 and 4 becomes so small that the temperature differences between cases 3 and 4 can not be seen in the macroscopic scale.

Figs. 6.4.11 and 6.4.12 show the temperature profiles on the vertical and the horizontal lines. While Fig.6.4.11 a) shows the temperature distribution in the melt under the crystal along the vertical line, $r = 1.125$ cm and $\theta = 0.0$ degree at the elapsed time t = 30.0 sec, Fig.6.4.11 b) shows the temperature distribution in the melt under the free surface along the vertical line, $r = 1.135$ cm and $\theta = 0.0$ degree at the elapsed time t = 30.0 sec. Fig.6.4.11 b) shows the temperature distribution in the melt under the crystal

along the horizontal line, r = 1.125 cm and θ = 0.0 degree at the elapsed time t = 30.0 sec, while Fig.6.4.11 b) shows the temperature distribution in the melt under the free surface along the horizontal, r = 1.135 cm and θ = 0.0 degree at the elapsed time t = 30.0 sec.

The effects due to the rotation of the crucible were not significantly observed for the temperature distribution except the horizontal temperature distribution at z =1.8 cm (Fig. 6.4.12 b)). On the contrary, the temperature is significantly suppressed by the presence of a magnetic field. As shown in Figs.6.4.11 and 6.4.12, the velocity has been already suppressed at the external magnetic field 1000.0 G. However, it can be also found that there are slight differences in the temperature distribution caused by the differences in the magnitudes of the magnetic field, particularly as depicted in Figs. 6.4.12 a) and b).

When the magnetic field is imposed on the melt, the flow velocity is reduced to a small magnitude. The effects due to the direction of an external magnetic field on the temperature field are not as significant as those on the flow field. Thus, while the non-axisymmetry was observed in the flow patterns when a magnetic field was imposed in the horizontal direction, the axisymmetry in the temperature distribution was observed.

As a result based on the comparison between cases without the rotation of the crucible, forced convection descends the large vortex created in the middle of the melt flow by natural convection to the center bottom of the crucible although natural convection is more dominant than the forced convection. On the other hand, the presence of a magnetic field drastically reduces both the velocity and the temperature. However, because of the dominant effects of the temperature field due to natural convection, the impact of the external magnetic field on the temperature field is not as significant as that observed on the velocity field.

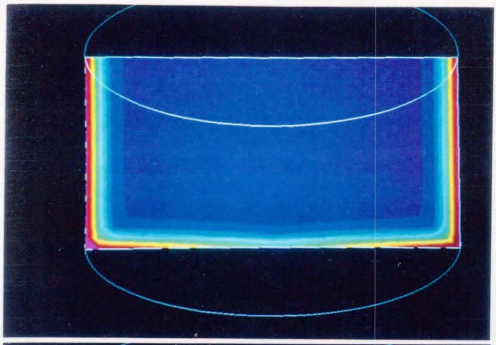

Fig.6.4.9 a)
t = 1.0 sec

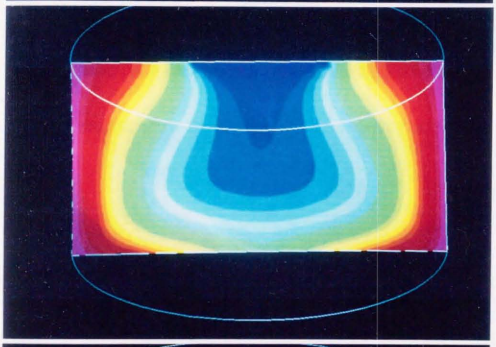

Fig.6.4.9 b)
t = 7.5 sec

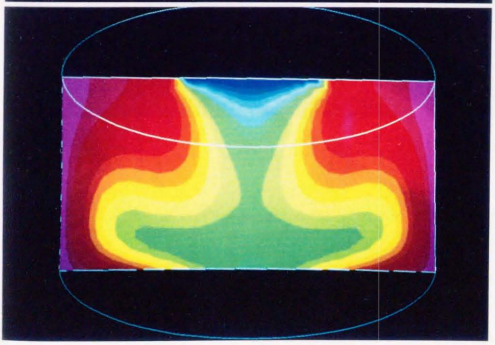

Fig.6.4.9 c)
t = 15.0 sec

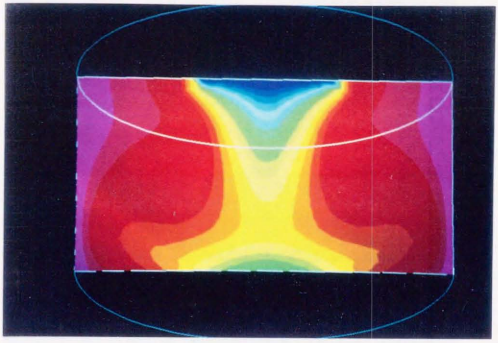

Fig.6.4.9 d)
t = 22.5 sec

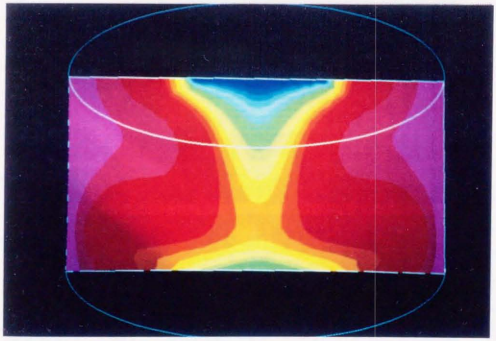

Fig.6.4.9 e)
t = 30.0 sec

Fig.6.4.9 Evolution of temperautreprofile on the verical plane for case 2

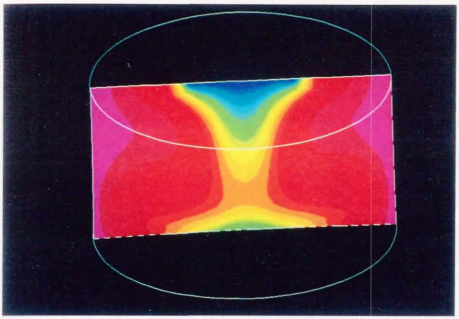

Fig.6.4.10 a)
Case 2
$B_x = 0$ G
$B_z = 0$ G

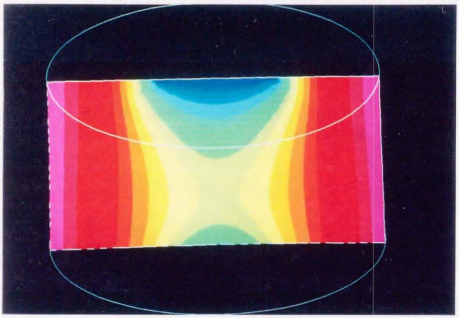

Fig.6.4.10 b)
Case 3
$B_x = 0$ G
$B_z = 1{,}000$ G

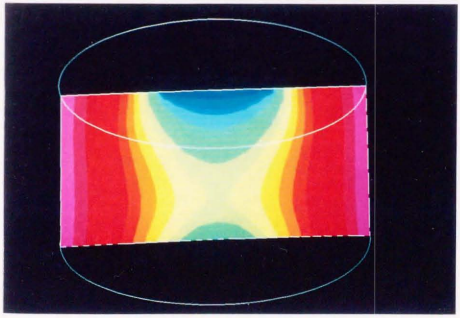

Fig.6.4.10 c)
Case 4
$B_x = 1{,}000$ G
$B_z = 0$ G

Fig.6.4.10 Temperature profile on the vertical plane at the elapsed time t = 30.0 sec

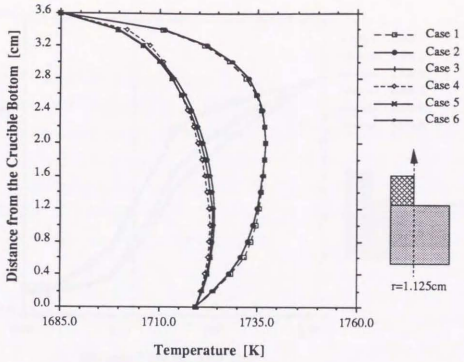

Fig. 6.4.11 a) Temperature profile on the vertical line at r = 1.125 cm andθ = 0.0 degree with respect to distance from the bottom

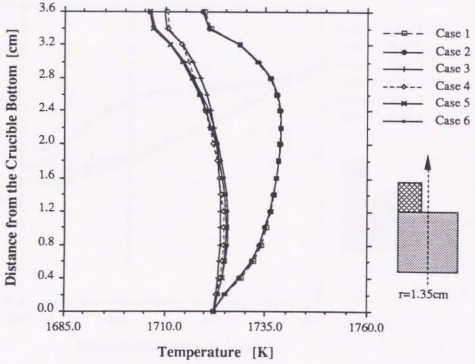

Fig. 6.4.11 b) Temperature profile on the vertical line at r = 1.35 cm andθ = 0.0 degree with respect to distance from the bottom

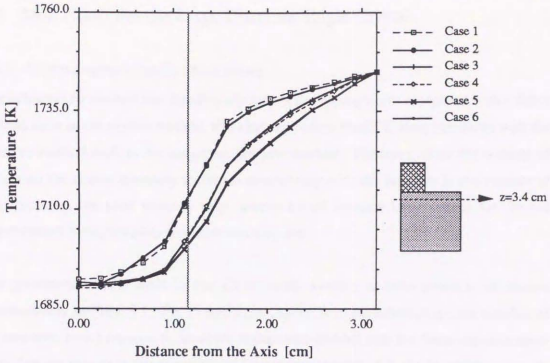

Fig.6.4.12 a) Temperature profile on the horizontal line at z = 3.4 cm and θ = 0.0 degree with respect to distance from the axis

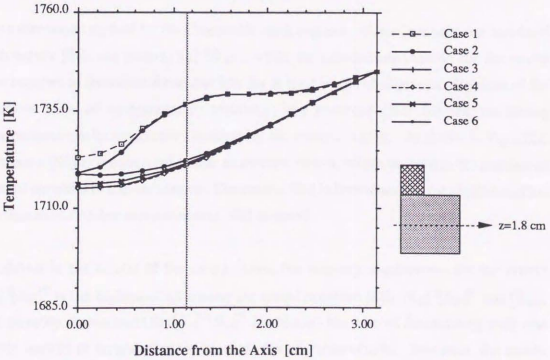

Fig.6.4.12 b) Temperature profile on the horizontal line at z = 1.8 cm and θ = 0.0 degree with respect to distance from the axis

6.5 Melt Flows For the Large-Diameter Single Crystal

6.5.1 Substructuring Mesh For Melt Flows

The substructure method can significantly reduce the memory size compared with a direct method such as the skyline method, and also can reduce the CPU time compared with the iterative method such as the conjugate gradient method. However, since the number of values on the shared boundary increases accordingly with the increase in the number of substructures, the total memory requirement would become large unless the further improvement is employed to minimize memory size.

The geometry of the melt in the Czochralski system is axisymmetric as shown schematically in Fig.6.5.1. For example, in case of four substructuring (the number of substructres, k=4) regions, an analysis region was divided into the finite element mesh such that the region is the assembly of four substructures with the identical geometry consisting of the internal values like ABCDEF, four side parts of the shared boundary regions like CGHFIJ and four central parts of boundary region like BOGEO'I [6.7].

The substructure method for the Czochralski melt requires to formulate only one matrix of each matrix [Sii] and matrix $[S_{ii}]^{-1}[S_{bi}]^T$, while the substructure method for the cavity flow requires to formulate those matrices for at least 3 x 3 substructures. Because of the characteristics of axisymmetric geometry, the matrices [Sii] for the remaining substructures can be obtained by multiplying the rotation matrix. As shown in Fig.6.5.2, the matrix [Sii] is the [m x m] sparse symmetric matrix, where m implies the number of internal variables in a substructures. The matrix [Sii] is formulated by the skyline method and then the LDU decomposed matrix [Sii] is stored.

As shown in the results of the cavity flows, the memory requirement for the matrix $[S_{ii}]^{-1}[S_{bi}]^T$ is the highest of all among the stored matrices [Sii], $[S_{ii}]^{-1}[S_{bi}]^T$ and $[\overline{S_{bb}}]$. The memory requirement for $[S_{ii}]^{-1}[S_{bi}]^T$ is reduced because of formulating only one matrix instead of formulating the matrices for all substructures. However, the matrix $[S_{ii}]^{-1}[S_{bi}]^T$ is becoming large, particularly for a large scale problem since a size of the matrix $[S_{ii}]^{-1}[S_{bi}]^T$ is [n x m], where n implies the total number of values on the shared

boundaries. Therefore, the further minimization in memory requirement for the matrix $[S_{ii}]^{-1}[S_{bi}]^T$ is carried out by taking into account the periodic regularity of the matrix due to the axisymmetric geometry. Since the only adjacent shared boundary region contributes to $[S_{ii}]^{-1}[S_{bi}]^T$, only corresponding adjacent side and central parts needs to be considered as shown in the shaded parts of Fig 6.5.2; 2). In addition, the parts appear periodically so that the remaining matrices $[S_{ii}]^{-1}[S_{bi}]^T$ can be calculated by multiplying the periodic matrices. Consequently, this would lead to a significant reduction in memory requirements.

The matrix $[\overline{S_{bb}}]$ is the size of [n x n] as illustrated in Fig.6.5.2; 3), where i implies the number of variables in the side part of a shared boundary, and j implies the number of variables in the central parts of a shared boundary. To the same extent, the configuration of the matrix $[\overline{S_{bb}}]$ is similar to that of the global matrix [S] although in a smaller scale. As the number of the substructures increases, the memory requirement for the matrix $[\overline{S_{bb}}]$ increases. If the entire [n x n] matrix is formulated, the ratio of increase in the number of substructures become linear to the number of the shared boundary variables squared. In order to prevent the large increase, the skyline method is applied to formulate matrix $[\overline{S_{bb}}]$. Furthermore, the LDU decomposed matrix of $[\overline{S_{bb}}]$ is stored so that the calculation of the shared boundary variables can be done by backward and forward substitution.

The bench mark test was conducted to assess the memory requirements and the CPU time requirements for the melts flows in the large diameter single crystal by varying the number of degrees of freedom. The simulations were performed by both the conjugate and substructure methods without an external magnetic field. The analysis model of Fig.6.2.1 were used with boundary conditions of Fig.6.3.1 for problems with three different cases in number of degrees of freedom (D.O.F) : 1) 40,000 D.O.F, 2) 140,000 D.O.F, and 3) 250,000 D.O.F. Geometric parameters and boundary conditions for each case are summarized in Table 6.5.1.

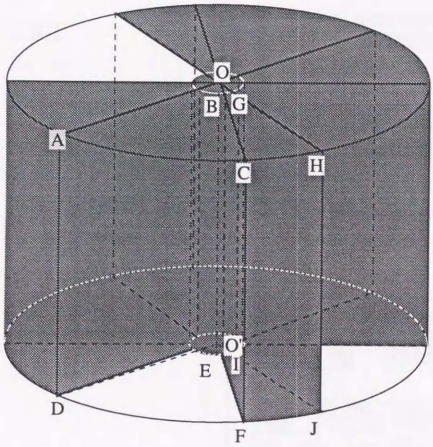

Fig.6.5.1 Schematic illustration of substructuring mesh division for melt flows during the Czochralski crystal growth of a single crystal

1) $[S_{ii}]$

:[m x m]
sparse symmetric matrix

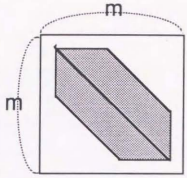

2) $[S_{bi}]$

$[S_{bi}] \cdot [S_{ii}]^{-1}$

:[n x m]
dense matrix with periodic regularity

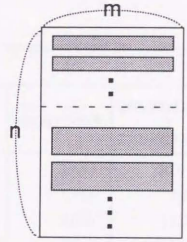

3) $[\overline{S_{bb}}]$

:[n x n]
dense symmetric matrix

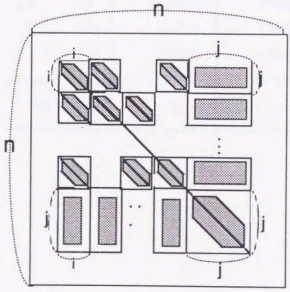

Fig. 6.5.2 Configuration of condensed out substructure matrices

Table 6.5.1 Geometry and boundary conditions of the temperature and the velocity

Parameters			40,000 D.O.F.	140,000 D.O.F. & 250,000 D.O.F.
Crucible Radius	(cm)	R_c	3.150	20.0 0
Crystal Radius	(cm)	R_s	1.125	7.14
Melt Depth	(cm)	H	3.600	12.00
Crystal / Melt Interface Temperature	(K)	T_s	1685.0	1685.0
Crucible Center Temperature	(K)	T_{cm}	1705.0	1700.0
Crucible Wall Temperature at the bottom	(K)	T_{wb}	1745.0	1745.0
Crucible Wall Temperature at the top	(K)	T_{wt}	1745.0	1694.0
Crystal Rotation Rate	(rpm)	Ω_s	30.0	15.0
Crucible Rotation Rate	(rpm)	Ω_c	– 15.0	– 5.0

6.5.2 Assessment of Memory Requirement and CPU Time

6.5.2.1 Memory Requirement

For a large scale problem, the most crucial issue is to satisfy the memory requirement. In order to simulate the melt for a six-inch diameter single crystal, the high number of mesh points would be indispensable. Therefore, the memory requirement has been estimated with respect to the number of degrees of freedom.

Table 6.5.2 summarizes the comparison of memory requirement for 40,000, 140,000 and 250,000 D.O.F. Although the analyses were performed on Cray computers whose maximum memory capacity is 1 giga bytes, it is more practical to keep the memory requirement less than 300 mega bytes for easy access to computation. The values in brackets in the Table 6.5.2 are the estimated ones. The reason for over estimation is because of over estimation in the size of the skyline matrix for the matrix $[S_{ii}]$.

The most efficient way to reduce the memory requirement is to minimize the memory size required for the matrix $[S_{ii}]^{-1}[S_{bi}]^T$ by increasing the number of substructures. However, there is the optimum relationship between the number of substructures and the memory usage because $[\overline{S_{bb}}]$ becomes large accordingly with the increase in the number of shared boundary values as seen in the cavity analysis.

As listed in Table 6.5.2, eight-substructure division can reduce its memory requirement to half the memory requirement for four-substructure division. From this reason, the melt flow for a large diameter crystal has been analyzed by the substructure method with an eight-substructure division.

Table 6.5.2 Comparison of memory requirements for melt flows

	40,000 D.O.F.		140,000 D.O.F.		250,000D.O.F.
	4 subs.	8 subs.	4 subs.	8 subs.	8subs.
Total No. of Nodes	8,670	8,075	28,923	28,055	50,375
Total No. of Elements	7,560	7,056	26,040	25,200	46,800
No. of Elements per Substructure	1,602	666	5,910	2,670	5,010
No. of Elements on the Shared Boundary	1,152	1,728	2,400	3,840	6,720
Memroty Requirement for $[S_{ii}]$ Matrix (MB)	1.232	0.222	10.060	2.095	6.967
Memory Requirement for $[\overline{S_{bb}}]$ Matrix (MB)	7.382	2.302	56.736	20.506	67.334
Memory Requirement for $[S_{bi}]\cdot[S_{ii}]^{-1}$ Matrix (MB)	4.729	7.246	20.450	34.698	101.928
Total Memory Requirement (Estimated Memory Requirement) (MB)	23.670 (24.2)	13.490 (15.6)	153.887 (179.6)	84.432 (97.5)	255.652 (321.9)

6.5.2.2 CPU Time

Similarly, the estimation and comparison for CPU time were conducted with respect to the number of degrees of freedom and are summarized in Table 6.5.3. The analyses were carried out on Cray Y-MP/8I from time step t = 0.0 to t = 1.0 with the size of time increment $\Delta t = 1.0 \times 10^{-3}$ expect the analyses for 250,000 D.O.F, which was done from t = 0.0 to t = 0.1.

The values in brackets in Table 6.5.3 are the estimated ones based on the results from the cavity flows. Since the memory size of the skyline matrix for the matrix $[S_{ii}]$ was overestimated, the CPU time was also overestimated. Regarding the CPU time, the large differences between the cavity flows and melt flows arose because the CPU time in cavity flow problems increases with an increase in the number of substructures, while the CPU time in the melt flows decreases with increase in an number of substructures.

Two reasons are considered to attribute to the reduction in CPU time against the increase in the number of substructures, as opposed to the relationship between CPU time and the number of substructures in the analysis of cavity flows. First of all, the number of degrees of freedom in the melt flow problem is one order larger than that in the cavity flow, which leads to more efficient vectorization. Secondly, in order to minimize the memory requirement for the matrix $[S_{ii}]^{-1}[S_{bi}]^T$, only the adjacent parts of the shared boundaries to the substructure are memorized by taking advantage of the axisymmetric geometry of the Czochlarski system instead of formulating the entire matrix $[S_{ii}]^{-1}[S_{bi}]^T$. In other words, the size of the matrix $[S_{ii}]^{-1}[S_{bi}]^T$ becomes independent of the number of substructures and the size is only effected by the number of internal variables. Therefore, in solving $\{\overline{f_b}\}$ and the internal values in the substructure $\{X_i\}$, the vector length for multiplication in terms of the matrix $[S_{ii}]^{-1}[S_{bi}]^T$ becomes shorter due to the reduction in the number of internal variables associated with increase in the number of substructures. Consequently, an eight substructure mesh is more efficient with regard to memory usage and CPU time.

Table 6.5.3 Comparison of CPU time required for melt flows

	40,000 D.O.F.		140,000 D.O.F.		250,000D.O.F.
	4 subs.	8 subs.	4 subs.	8 subs.	8subs.
Total No. of Nodes	8,670	8,075	28,923	28,055	50,375
Total No. of Elements	7,560	7,056	26,040	25,200	46,800
No. of Elements per Substructure	1,602	666	5,910	2,670	5,010
No. of Elements on the Shared Boundary	1,152	1,728	2,400	3,840	6,720
CPU Time Requirement for Matrix Formulation (sec)	49.0	68.6	398.5	562.6	1,606.6
CPU Requirement for Solver [t=0.0 ~ 1.0] (sec)	1,309.0	1,036.8	7,553.0	6,336.8	1,766.8 *1
Total CPU Time (Estimated CPU Time) [t=0.0 ~ 1.0] (sec)	1,364.4 (1,411.1)	1,111.4 (1,941.8)	7,980.5 (8,377.9)	6,926.7 (10,315.8)	3,419.4 *1 (35,073.7)

*1 Total time step is 100 from t = 0.0 to t = 0.1

* Size of time step = 1.0×10^{-3}

* The analyses were performed on Cray Y-MP/8I

6.5.2.3 Comparison with the Conjugate Gradient and the Skyline Methods

The memory and CPU requirements for the substructure method are compared with those for the skyline and the conjugate gradient (CG) methods, where the former is a widely used direct method, and the latter is a widely used iterative method. Table 6.5.4 summarizes the results with respect to the number of degrees of freedom. For analyses by the conjugate gradient method, the finite element mesh for eight substructures were used.

The skyline method stores the entire global matrix while the conjugate gradient method is feasible to solve the finite element matrix without storing the entire global matrix. The skyline method requires 11 giga bytes of memory even for 40,000 D.O.F problem due to storage of the entire global matrix. On the contrary, the conjugate gradient method does not require a large amount of memory size due to no formulation of the global stiffness matrix. However, the CPU time becomes quite large because the global matrix has to be formulated at each CG iteration at each time step. It is recognized that the number of CG iterations increases linearly with the increase in the number of degrees of freedom squared, so that the constraint on CPU time becomes an obstacle for melt flow analyses which require more than 10,000 time steps to observe significant behavior of the melt flow.

Table 6.5.5 concludes the comparison of memory and CPU time requirements for three methods when the values for the substructure method with eight substructures are taken as the basis values. The substructure method requires 1/1,000 of memory size compared with the skyline method, and 1/5 of CPU time compared with the conjugate gradient method.

The correlation between the number of degree of freedom and the CPU time was derived for the substructure method and the conjugate gradient method, based on the assessment of CPU time.

The correlation can be expressed qualitatively as follows.

For the conjugate gradient method:

$$\mathrm{CPU(CG)} = N_{el} \times \left[N_{ts} \times \left(a_{cg} \times N_{it} + b_{cg} \right) + c_{cg} \right] , \qquad (6.5.1)$$

For the substructure method:

$$\begin{aligned} \mathrm{CPU(SUB)} &= N_{el} \times \left[N_{ts} \times a_{st1} + b_{st1} \right] \\ &= N_{sb} \times \left[N_{ts} \times a_{st2} + b_{st2} \right] \\ &= N_{bc} \times \left[N_{ts} \times a_{st3} + b_{st3} \right] , \end{aligned} \qquad (6.5.2)$$

where N_{el} , N_{sb} and N_{bc} denote the total number of elements, the number of internal values in a substructure, and the number of values on the shared boundaries, respectively. In Eqs. (6.5.1) and (6.5.2), N_{ts} and N_{it} denote the number of time steps and the number of CG iteration. The letters a and b are the coefficients for each method, depending on the capability of a computer.

In general, the number of the CG iterations increases as the number of degrees of freedom increases. Therefore, the increase in CPU time can be assumed to be a power function of the increase in the number of degrees of freedom to n-th degree. On the contrary, since the substructure is calculated by the direct method, the increase in CPU time can be assumed to be linear with the size of the skyline matrix, which varies depending on the number of substructures.

As a result, the correlation for the CPU time requirement for the conjugate gradient and the substructure methods are estimated as follows.

For the conjugate gradient method:

$$\text{Increase in CPU(CG)} \approx (\text{Increase in D.O.F.})^{1.5\sim1.8} . \qquad (6.5.3)$$

For the substructure method:

4 substructures:

$$\text{Increase in CPU(SUB)} \approx (\text{ Increase in D.O.F.}) \times 1.7\sim1.9 \qquad (6.5.4)$$

8 substructures:

$$\text{Increase in CPU(SUB)} \approx (\text{ Increase in D.O.F.}) \times 1.5\sim1.7 \qquad (6.5.5)$$

Thus, increase in CPU time for the conjugate gradient method can be assumed to scale as a 1.5-th to 1.8-th power function of the increase in the number of degrees of freedom. In contrast, increase in CPU time for the substructure method with four substructures can be assumed to scale linearly as 1.7 to 1.9 times the increase in the number of degrees of freedom, while that with eight substructures is assumed to scale as 1.5 to 1.7 times the increase in the number of degrees of freedom.

Table 6.5.4 Summary of memory size and CPU time required for the substructure, the skyline and the conjugate gradient methods with respect to the number of degrees of gfreedom

No.of Degrees of Freedom	Size of Global Matrix	Memory Requirement (MB)			CPU Time (sec)		
		Substructure Method		CG Method	Substructure Method		CG Method
		4	8		4	8	
40,000	11G	23.7	13.5	8.3	1,364.0	1,111.4	6,461.1
125,500	91G	153.9	84.4	28.6	7,980.5	6,926.7	32,841.9
250,000	303G	-	255.7	51.2	-	3,419.4 *1	-

*1 Total time step is 100 from t = 0.0 to t = 0.1

* Size of time step = 1.0×10^{-3}

* The analyses were performed on Cray Y-MP/8I

Table 6.5.5 Comparison of ratios of increase in memory requirement and CPU time for the substructure method with eight substructures, the skyline and the conjugate gradient methods

	Skyline Method	Substructure Method (8 Substructures)	Conjugate Gradient Method
Memory Requirement	× 1,000	1	× 0.2
CPU Time	-	1	× 5

Note: Each value is normalized by the value of substructure method

6.5.3 Analysis Parameter Description

In this section, the melt flows in the Czochralski growth of a six-diameter single crystal were analyzed.

The memory requirements for four division of the substructure method is more than 500 mega bytes according to the assessment in Chpater 6.4, and this memory requirement is quite demanding even on the Cray super computer. Therefore, an eight substructure division was used for the analyses. Fig. 6.5.3 shows the finite element mesh used for the analysis by the substructure method with an eight-substructure division. The mesh division consists of 50,375 and of total number of 46,800 nodes as described in Fig.6.5.3. The analysis region has been divided into elements to discretize the melt depth with $\delta z = 0.4$ cm length in the z-direction and the radial direction with $\delta r = 0.7$ cm length.

Table 6.5.6 summarizes the geometric parameters and operating conditions for the temperature and the velocity. The boundary conditions were employed basically by the same manner to those for the analysis of small-size crystal by referring the values of the parameters to the reference [6.6]. However, the thermal boundary condition on the crucible wall was given in a different way. For the small diameter crystal, the temperature boundary conditions on the crucible wall were given by a constant value. On the other hand, for the larger diameter crystal, the temperature distributions on the crucible wall were given by a linear function of melt depth from the bottom since the larger the system becomes, the more difficult it would become to keep the wall temperature at the constant value. The values of the thermal boundary conditions were referred to the references [6.4] and [6.7].

The analyses were conducted with the same physical properties used for the analyses of the small size single crystal except the kinematic viscosity and the volumetric expansion coefficient. The kinematic viscosity and the volumetric expansion are used to calculate the non-dimensional numbers such as the Reynolds or the Rayleigh number, which is indicates the qualitative behavior of the flow. If the listed values in Table 6.4.1 were used, the Reynolds and the Rayleigh numbers would result in about 1.0×10^5. This implies that the melt flow would show turbulent behavior and it would become difficult to obtain the converged results without consideration of the turbulent model. Therefore, the

analyses used the kinematic viscosity and volumetric expansion coefficient with 1/100-th of the values of both parameters listed in Table 6.4.1.

For the initial conditions, the melt was assumed to be at the quiescent state. Thus, all initial conditions for the velocity, the pressure, and the electric potential are set to be zero. The initial conditions for the temperature are set to be at 1690 K. Then, the melt flow was analyzed with the time increment size $\Delta t = 1.0 \times 10^{-3}$ from the elapsed time t = 0.0 sec to t = 15.0 sec and $\Delta t = 2.0 \times 10^{-3}$ from t = 15.0 sec to t = 30.0 sec.

Table 6.5.6 Geometric parameters and boundary conditions of the velocity and temperature for melt flow simulations of six-inch diameter silicon crystal

Parameters			6 inch
Crucible Radius	(cm)	R_c	20.00
Crystal Radius	(cm)	R_s	7.14
Melt Depth	(cm)	H	12.00
Crystal / Melt Interface Temperature	(K)	T_s	1685.0
Crucible Center Temperature	(K)	T_{cm}	1700.0
Crucible Wall Temperature at the bottom	(K)	T_{wb}	1745.0
Crucible Wall Temperature at the top	(K)	T_{wt}	1694.0
Crystal Rotation Rate	(rpm)	Ω_s	15.0
Crucible Rotation Rate	(rpm)	Ω_c	– 5.0

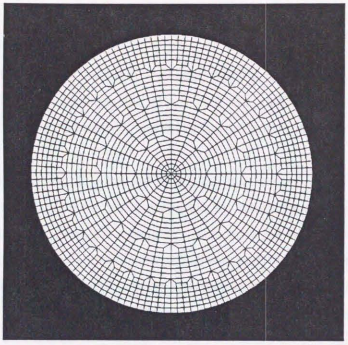

a) Horizontal view of the finite element mesh in the melt region

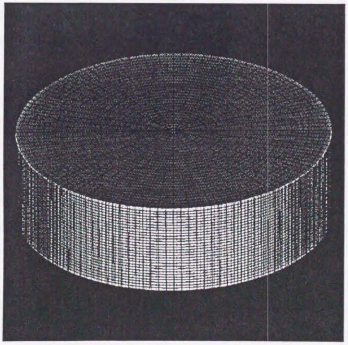

b) Detailed view of the finite element mesh in the melt region

Fig.6.5.3 Finite element meh in the melt region
(total number of elements = 46,800, total number of nodes = 50,375)

6.5.4 Analysis Results

6.5.4.1 Flow patterns

The evolution of the velocity field on the vertical plane is described in Figs.6.5.4 a) and b) at the elapsed time t= 15.0 sec and at t = 30.0 sec, respectively. The velocity is depicted at the 25 points in the radial direction by interpolating the nodal values.

The flow in the melt are initially caused by natural convection. The thermal boundary conditions are given such that the crucible wall has the temperature distribution as a linear function of the distance from the crucible bottom with 40 K temperature difference between highest temperature at the bottom and lowest temperature at the top, and bottom part of the crucible has higher temperature distribution than the crystal. Therefore, the melt flows in the inward direction as the time proceeds. Thus, the vortex due to this effect, primarily by natural convection can be observed under the free surface.

Figs.6.5.6 a) and b) plot the circumferential velocity distribution along the vertical line at three points at the elapsed time t = 15.0 sec and t = 30.0 sec, respectively in order to see detailed flow behavior in the characteristic region such as near the crystal, the free surface, or the crucible. As the schematic figure in the figures illustrates, the curves (1) --•-- shows the flow velocity under the crystal, the curve (2) —×— shows the flow velocity under the free surface close to the the crystal, and the curve (3) —□— shows the flow velocity under the free surface close to the crucible.

On the other hand, Figs. 6.5.7 a) and b) describe the circumferential velocity distribution along the horizontal line at time t = 15.0 sec and t = 30.0 sec, respectively. The plotted region have been chosen to see behavior near the crystal/melt interface ((1) --•--), the center of the melt ((2) —×—), and near the crucible ((3) —□—).

As shown in figures, the velocity in the bulk region are not varied much with an increase in time as compared with that in the region close to the boundary. In particular, the curve (1) in Fig.6.5.6 b) shows the evolution of the velocity field.

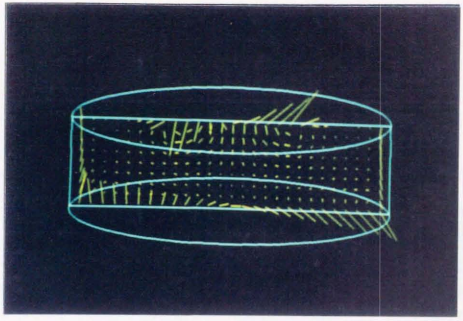

Fig.6.5.4 a)
t = 15.0 sec

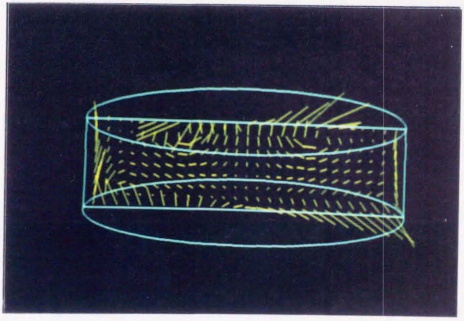

Fig.6.5.4 b)
t = 30.0 sec

Fig.6.5.4 Evolution of velocity profile on the vertical plane

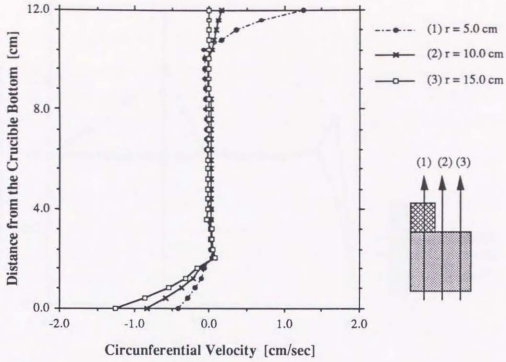

Fig.6.5.5 a) Circumferential velocity profile on the vertical line at $\theta = 0.0$ degree with respect to distance form the axis at the elapsed time t = 15.0 sec

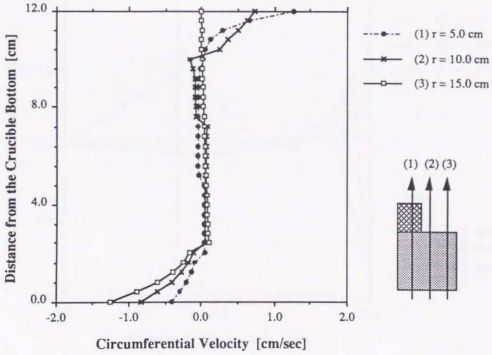

Fig.6.5.5 b) Circumferential velocity profile on the vertical line at $\theta = 0.0$ degree with respect to distance form the axis at the elapsed time t = 30.0 sec

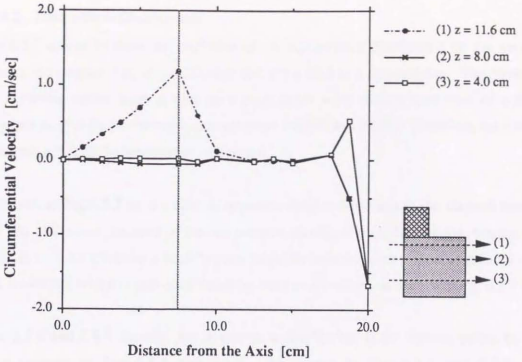

Fig.6.5.6 a) Circumferential velocity profile on the vertical line at θ = 0.0 degree with respect to distance form the axis at the elapsed time t = 15.0 sec

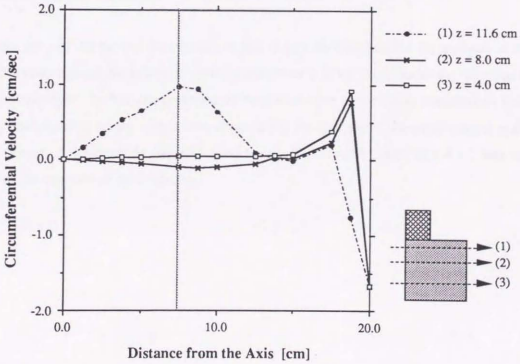

Fig.6.5.6 b) Circumferential velocity profile on the vertical line at θ = 0.0 degree with respect to distance form the axis at the elapsed time t = 30.0 sec

6.5.4.2 Temperature Distributions

Figs.6.5.7 a) and b) show the evolution of the temperature distribution on the vertical plane at the elapsed time at t = 15.0 sec and at t = 30.0 sec, respectively. The colors of the isotherm varies from a blue to a pink color with twenty variation of colors, corresponding to the temperature changes from 1685 K to 1745 K. Therefore, each color represents a 3 K of the temperature increment.

As shown in Fig.6.5.7 a), the cold temperature field is dominant at the elapsed time t= 15.0 sec. However, because of the temperature distribution on the crucible bottom and the wall, bulk temperature gradually rises from the outer to inner region associated with time evolution, which is primarily cased by natural convection as shown in Fig.6.5.7 b).

Figs. 6.5.8 and 6.5.9 describe the temperature distribution at the various points by the same manner in Figs.6.5.5 and 6.5.6. As shown in Figs.6.5.8 and 6.5.9, the temperature rise associated with the time evolution has been observed, particularly at the region close to the crucible wall, such as the regions plotted by the curve (3) in Fig.6.5.8 and the curve (3) in Fig.6.5.9.

Since the ratio of the melt to the crucible radius is smaller than that for the analysis of the small diameter crystal, the effect of natural convection is much more dominant than that of forced convection. In fact, the temperature striations were observed as temperature rose. On the other hand, a vortex which were observed in the analysis of the small crystal at the upper corner of the crucible due to forced convection crystal (see Fig.6.4.2) was not found in the analysis of the large one.

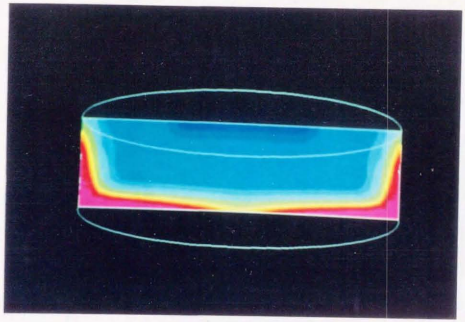

Fig.6.5.7 a)
t = 15.0 sec

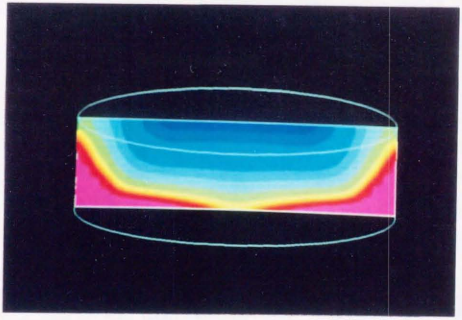

Fig.6.5.7 b)
t = 30.0 sec

Fig.6.5.7 Evolution of temperature distribution on the vertical plane

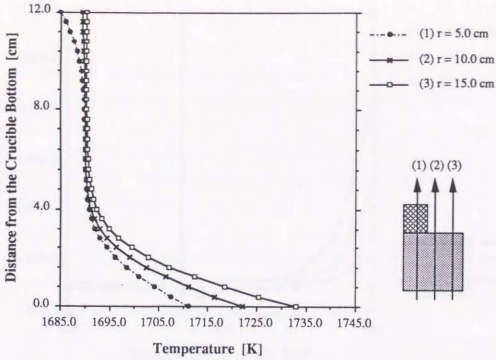

Fig.6.5.8 a) Temperature profile on the vertical line at $\theta = 0.0$ degree with respect to distance form the axis at the elapsed time t = 15.0 sec

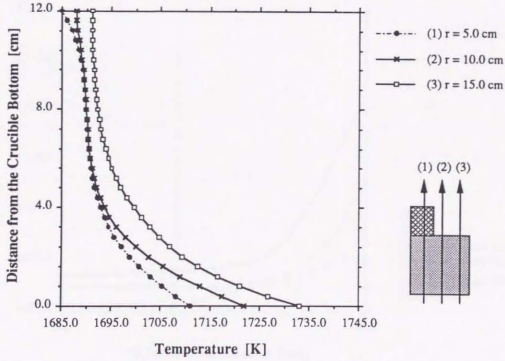

Fig.6.5.8 b) Temperature profile on the vertical line at $\theta = 0.0$ degree with respect to distance form the axis at the elapsed time t = 30.0 sec

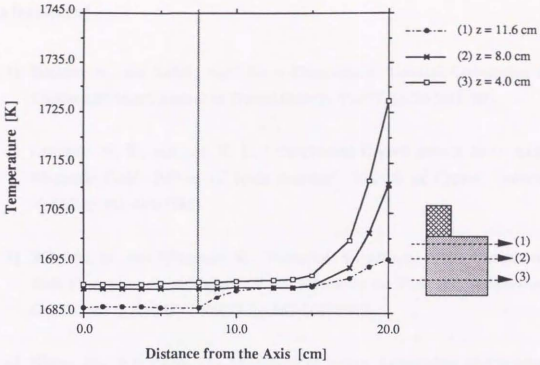

Fig.6.5.9 a) Temperature profile on the horizontal line at $\theta = 0.0$ degree with respect to distance form the axis at the elapsed time t = 15.0 sec

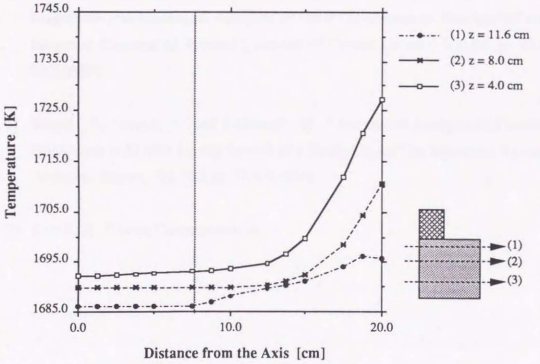

Fig.6.5.9 b) Temperature profile on the horizontal line at $\theta = 0.0$ degree with respect to distance form the axis at the elapsed time t = 30.0 sec

[References]

[6. 1] Bottaro, A., and Zebib, A., " Three-Dimensional Thermal Convection in Czochralski Melt", Journal of Crystal Growth, Vol.97, pp.50-58(1989).

[6. 2] Langolis, W. E., and Lee, K. J., " Czochralski Crystal growth in an Axial Magnetic Field: Effects of Joule Heating", Journal of Crystal Growth, Vol.62,pp.481-486(1983).

[6. 3] Mihelcic, M., and Wingerath, K., "Numerical Simulations of the Czochralski Bulk Flow in an Axial Magnetic Field: Effects on the Flow and Temperature Oscillations in the Melt", Vol.71, pp.163-168(1985).

[6. 4] Hirata, H., Ph.D thesis, The University of Tokyo, Department of Electrical Engineering (in Japanese) (1991).

[6. 5] Cartwright, R., Ilegbusi, O. J., and Szekely, J., " A Comparison of Order-of-Magnitude and Numerical Analyses of Flow Phenomena in Czochralski and Magnetic Czochralski Systems", Journal of Crystal Growth, Vol.94, pp.321-333(1989).

[6. 6] Sawada, I., Tanaka, M., and Nakamura, M., " Numerical Analysis of Thermal Convection in Si Melt During Growth of a Single Crystal" (in Japanese), Yawata Technical Report, Vol.330, pp.37-43(1988).

[6. 7] Kawai, H., Private Communication.

Chapter 7

Summary and Discussion

7.1 Summary and Discussion

This chapter summarizes the analysis results and discusses future recommendations based on the knowledge obtained by the analysis results.

A numerical analysis program has been developed to analyze the transient magneto-thermal-hydrodynamic flow in three-dimensions, primarily for the Czochralski melt growth of a single crystal. In the analysis of the transient three-dimensional problem, the effective usage of memory and the minimization of CPU time are emerging problems. In order to improve these computational performance parameters, the substructure method was applied to the pressure Poisson equation which was derived from the MAC (Marker And Cell) time integration scheme.

7.1.1 Analysis of Cavity Flows

The cavity flows were first analyzed to demonstrate the applicability of the substructure method. The analysis aims to examine three aspects of the computational performance: 1) accuracy, 2) memory requirement, and 3) CPU time. The simulation were conducted by dividing the analysis region with the total number of 5,041 elements and 10,368 nodes with the various number of substructures.

The accuracy of the analysis results were compared with the computational results by Ghia [7.1] for a Reynolds number, Re =100 and good correlation was obtained. Since the substructure method updates the shared boundary values in a direct way as opposed to an iterative way by the domain decomposition method, differences in dividing the analysis region or in the number of substructures were found not to affect the accuracy of the computational results.

Memory usage and CPU time required for the substructure method were compared with those for the conjugate gradient method. The results showed that if the analysis region was divided into more than 3 x 3 substructure divisions in the x- and the y- directions, memory size requirements were reduced. Since in the case of 3 x 3 substructure division, the geometry and the boundary conditions differ in each substructure, all condensed-out substructure matrices must be stored. However, for the cases of more than 3 x 3 substructure division, there are some substructures with an identical geometry and an identical boundary condition so that it is not necessary to store all condensed-out substructure matrices, which leads to the reduction in memory size as seen in case of over 3 x 3 substructure division.

In the conjugate gradient method, the global matrix is reformulated at each iteration step of the conjugate gradient method and at each time step, a large amount of CPU time is required. On the other hand, in the substructure method, once the condensed-out substructure is stored, it is not necessary to calculate and formulate the global matrix. Therefore, the calculation can be done by the forward and backward substitution. Consequently, it requires less CPU time than the conjugate gradient method as shown in the analysis results. The CPU time remained almost constant value up to 4 x 4 substructure division although it gradually increased for the case of 6 x 6 substructure division.

Consequently, the advantages and disadvantages of the substructure method can be summarized as follows.

Advantages:

* Accuracy is independent of the number of substructures because the shared boundary values can be obtained in a directly.

* Incompressibility in the substructure is satisfied because the substructure method simply solves the rearranged global matrix.

* CPU time is reduced compared with an iterative method, such as the conjugate

gradient method because once the condensed-out substructure matrices are formulated, the calculation can be done by backward and forward substitution without reformulating the entire global matrix at each time step.

Disadvantages:

* Application is limited to the specific configuration of the analysis region such as an assembly of substructures with identical geometry and boundary conditions because if the condensed-matrix is different in substructures, it requires to store all of the corresponding substructure matrix , which leads to the increase in memory usage.

* There is the optimum number of substructures because the number of shared boundary values increases accordingly with the increase in the number of substructures, resulting in the increase in the total memory requirement.

Since the Czochralski crucible is an axisymmetric configuration, it can be divided into a number of substructures with identical geometry an associated boundary conditions. In addition, the analysis region is not necessary to be divided into a large number of substructures otherwise the width of the substructure becomes too thin to be analyzed. In this sense, the substructure method can be effectively applied to the analysis of melt flows. The further improvement has been done for the melt flow analysis by taking advantage of the axisymmetric characteristics of the crucible geometry. As a result, the memory requirement was drastically reduced.

7.1.2 Analysis of Melt Flows for the Small Diameter Single Crystal

The melt flow during the Czochralski crystal growth was analyzed for a small size single crystal whose diameter is one inch. Analyses were conducted by varying the operating parameters such as rotation rate of the crystal and the crucible, and also magnitude and direction of an external magnetic field.

It was found that the forced convection caused by the rotation of the crucible did not give a significant impact on the temperature field. However,the velocity and the temperatures were dramatically suppressed when the magnetic field was imposed at a magnitude of 1,000 G (magnetic field flux density) in either the vertical or the horizontal direction. Especially, non-axisymmetric flow patterns were observed when the magnetic field was imposed in the horizontal direction. However, the temperature field did not show significant non-axisymmetric distribution in case of the horizontal external magnetic field. The reason of this temperature behavior is that the changes in the velocity field depending on imposing magnetic direction was not big enough to affect the temperature distribution in macroscopic scale due to dominant effects of natural convection on the temperature field.

Because of the dominant effects due to the natural convection, the melt flow behavior is quite sensitive to the thermal boundary conditions, and therefore, the thermal boundary conditions require the careful considerations.

7.1.3 Analysis of Melt Flows for the Large Diameter Single Crystal

The requirements for memory requirement and CPU time in the melt analysis of the large-diameter expect to become quite demanding. Therefore, the substructure method was introduced. Before the melt flow was analyzed, the assessment of memory size and of the CPU time was conducted.

The memory and CPU requirements for the substructure were compared with those for the skyline method and the conjugate gradient (CG) method, where the former was an example of the direct method, and the latter was an example of the iterative method.

The skyline method stores the information about the global matrix, while the conjugate gradient method solves the finite element matrix without storing the information about the global matrix. The skyline method requires 11 giga bytes of memory even for a 40,000 D.O.F problem due to memorization of the global matrix. On the contrary, the conjugate gradient method does not require a large amount of memory size due to no formulation of the global stiffness matrix. However, the CPU time becomes quite large because the global matrix has to be formulated at each CG iteration at each time step. It is recognized

that the number of CG iteration increases in the ratio of approximately square times of increase in the number of degrees of freedom, so that the constraint on CPU time becomes an obstacle for a melt flow to require more than 10,000 time steps to observe significant behavior of the melt flow.

The substructure method requires 1/1,000 of memory size compared with the skyline method, and 1/5 of CPU time compared with the conjugate gradient method.

The correlation between the number of degrees of freedom and the CPU time was derived for the substructure method and the conjugate gradient method, based on the assessment of CPU time.

The correlation can be expressed qualitatively as follows.

For the conjugate gradient method:

$$CPU(CG) = N_{el} \times \left[N_{ts} \times \left(a_{cg} \times N_{it} + b_{cg}\right) + c_{cg}\right] . \qquad (7.1.1)$$

For the substructure method,

$$\begin{aligned} CPU(SUB) &= N_{el} \times \left[N_{ts} \times a_{st1} + b_{st1}\right] \\ &= N_{sb} \times \left[N_{ts} \times a_{st2} + b_{st2}\right] \\ &= N_{bc} \times \left[N_{ts} \times a_{st3} + b_{st3}\right] \end{aligned} \qquad (7.1.2)$$

where N_{el} , N_{sb}, and N_{bc} denote the total number of elements, the number of internal values in a substructure, and the number of values on the shared boundaries, respectively. And, N_{ts} and N_{it} denote the number of time steps and the number of CG iteration. The letters a and b are the coefficients for each method, depending on the computer.

The number of the CG iteration increases as the number of degrees of freedom increases. Therefore, the increase in CPU time can be assumed to be a power function representing the number of degrees of freedom to n-th degree. On the contrary, since the substructure

solver is the direct method, increase in CPU time can be assumed to be linear with the size of the skyline matrix, which varies the number of substructures.

As a result, the correlation for the CPU time requirement for the conjugate gradient and the substructure methods are estimated as follows.

For the conjugate gradient method:

$$\text{Increase in CPU(CG)} \approx (\text{Increase in D.O.F.})^{1.5\sim1.8} \qquad (7.1.3)$$

For the substructure method:

4 substructures

$$\text{Increase in CPU(SUB)} \approx (\text{ Increase in D.O.F.}) \times 1.7\sim1.9 \qquad (7.1.4)$$

8 substructures

$$\text{Increase in CPU(SUB)} \approx (\text{ Increase in D.O.F.}) \times 1.5\sim1.7 \qquad (7.1.5)$$

Thus, increase in CPU time for the conjugate gradient method can be assumed to scale as a 1.5- th to 1.8- th power function of the increase in the number of degrees of freedom. In contrast, increase in CPU time for the substructure method with four substructures can be assumed to scale linearly as 1.7 to 1.9 times the increase in the number`of degrees of freedom, while that with eight substructures is assumed to be between 1.5 and 1.7 times the increase in the number of degrees freedom.

Based on the assessment, the eight-substructure with the total number of 46,800 elements and of 50,375 nodes were use to analyze the melt flow for the large diameter single crystal. Because of the substructure method, the required CPU time was reduced to 1.5 days for 10,000 time steps in which the conjugate gradient method takes about one week.

The dominant effects of the natural convection was observed compared with those of the

forced convection. In the melt, there is Marangoni convection due to surface tension of the free surface. However, as the diameter becomes large, the effects of Marangoni is considered to become small. For the large melt analysis, it is more important to consider turbulent behavior of the melt rather than the effects of Marangoni convection. In fact, the analysis could obtain the converged value when it used 1/100 of the original values of the kinematic viscosity and the volumetric expansion coefficient because of the high Reynolds and Rayleigh numbers.

If the turbulent model such as the k-ε model is introduced in order to solve the turbulent flow, the number of the considered variables increases. However, if the turbulent kinematic energy k and the turbulent kinematic dissipation rate ε are discretized in the explicit manner as the temperature T, which is solved by discretizing the energy equation explicitly, the substructure method is valid to solve the melt flow at the turbulent state.

7.3 Recommendations

In the melt flow analyses, it is found that the effects due to the natural convection is quite dominant. Therefore, the thermal conditions need to be considered carefully. The best way would be to incorporate in the global model in the way that the result from the global model can be used as the boundary conditions for the melt flow analysis.

As the system becomes larger, the Reynolds and Rayleigh numbers increase. Particularly, the turbulent flow would be caused by the high Rayleigh number because of the high temperature. Therefore, it is important to include the turbulent model.

In order to pursue the further memory minimization in the substructure method, the size of condensed out shared boundary matrix $[\overline{S_{bb}}]$ needs to be reduced. For the Czochlarski melt flow analysis, the further minimization of memory size required for the matrix $[\overline{S_{bb}}]$ can be done by using the periodic characteristics of the matrix due to the axisymmetric geometry of the Czochralski.

The substructure method is inherently suitable for the parallel processing in the sense that

the analysis of each substructure can be done individually due to division of the analysis region. Therefore, in order to reduce the CPU time requirement, it is efficient to develop the algorithm which takes advantage of the parallel processing.

[Reference]

[7. 1] Ghia, U., Ghia, K. N., and Shin, C. T., " High-Re Solutions for Incompressible Flow Using the Navier-Stokes Equations and a Multigrid Method", Journal of Computational Physics, Vol.48, pp.387-411(1982).

Chapter 8

Conclusions

The thesis has aimed to develop a numerical analysis program for large scale problems of transient magneto-thermal-hydrodynamic flows in three-dimensions and to simulate the melt flows during the Czochralski growth of a single crystal.

In order to improve computer performance such as memory requirements and CPU time in solving large scale problems, the substructure method was proposed. The performance of the substructure method was evaluated by comparing the results with those of the conjugate gradient method.

The analyses of melt flows during the Czochralski growth were conducted for both small- and large-diameter single crystals by the conjugate gradient method and by the substructure method. The flow and temperature behavior of the melt were studied by varying the operating conditions such as the rotation rate of crystal and crucible, and the magnitudes and directions of external magnetic fields.

The conclusions of the thesis can be summarized as follows.

1). Transient magneto-thermal-hydraulic flow problem requires a quite large number of memory due to the calculation of six variables. Application of the substructure method resulted in 1/1000 reduction in memory size compared to that of the skyline method.

2) The conjugate gradient method is not practical for transient problem in terms of CPU time due to iteration at each time step. Application of the substructure method resulted in 1/5 reduction in total CPU time compared to that of the conjugate gradient method.

3) The analyses of melt flows show that the natural convection is more dominant than the forced convection. It is observed that an imposed magnetic field can suppress temperature profiles by 30 degrees in 1000 gauss magnetic field.

Because of the rapid improvement in computer technology and computational techniques, the role of numerical analysis will become more important in the areas of fluid dynamics and melt crystal growth. It would be quite rewarding that the thesis could contribute to the future research in these fields as one of mile stones.

Acknowledgments

I am very thankful that I was given an opportunity to study and to do research at the University of Tokyo. Whole experiences here at the University of Tokyo gave tremendous impacts on my life in many aspects.

First of all, I would like to thank professor Genki Yagawa and Professor Shinobu Yoshimura for their helpful and patient guidance in supervising my thesis. I wish to thank Professors Hiroshi Okuda and Yasuhiro Akahoshi, and Drs. Naoki Soneda, Akira Yoshioka and Masahiko Kuroki for practical advice and discussion in numerical analyses even after their graduation.

I would like to thank Mr. Hiroshi Kawai for his generous assistance to provide pre- and pro-processing programs for my analysis, and also to thank Mr. Kiwame Tokai for discussion in computational fluid dynamics. My deep appreciation goes to Mr. Hirotoshi Hishida for his encouragement to write thesis, and to Messrs. Yasumi Kitajima, Yoshihiko Mochizuki, Chang-Ryul Pyo, Ms. Min-Yan Zhang, Messrs. Takahiro Oishi, Ryuji Shioya, Seichiro Hamada, and Per Kjellgren to make my Todai life enjoyable. I also would like to thank Ms. Kozue Chiba and Kayoko Amamiya for their kind assistance.

I appreciate professors Takeo Fukuda, Keigo Hoshikawa at Tohoku University and Professor Noriyuki Miyazaki at Kyushu University for their helpful advice in the melt growth. I also would like to thank Messrs. Kazumasa Fujioka and Shinji Sakata to provide helpful information and materials for my thesis.

I also want to thank all my friends in Japan and also in the U.S.A. who encouraged me to go thorough tough times. Finally, I wish to appreciate my family, especially, my parents for their support throughly as I pursued my study for almost ten years.

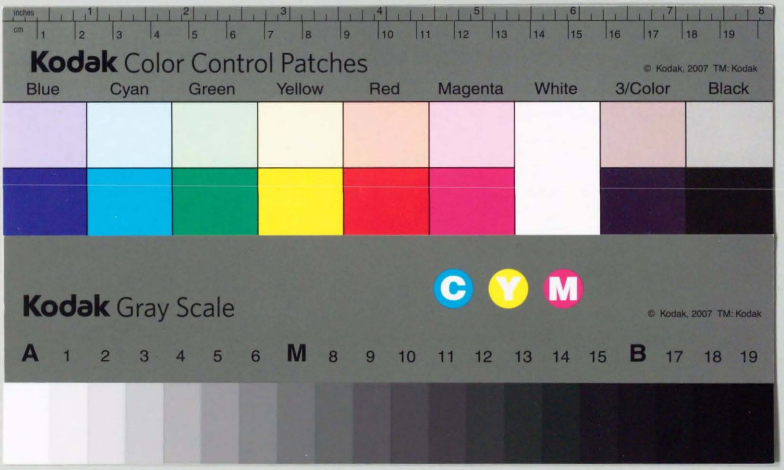
inches
cm
Kodak Color Control Patches
© Kodak, 2007 TM: Kodak
Blue
Cyan
Green
Yellow
Red
Magenta
White
3/Color
Black
C
Y
M
Kodak Gray Scale
© Kodak, 2007 TM: Kodak
A 1 2 3 4 5 6 M 8 9 10 11 12 13 14 15 B 17 18 19